Fatigue strength of additively manufactured 316L austenitic stainless steel

Punit Kumar[1], R. Jayaraj[1], J. Suryawanshi[2], U.R. Satwik[1], J. McKinnell[3], U. Ramamurty[1*]

[1]School of Mechanical and Aerospace Engineering, Nanyang Technological University, Singapore, 639798, Republic of Singapore
[2]Innovae3D Pvt. Ltd., Chakan, 410501, Pune, India
[3]HP Inc., 1070 NE Circle Blvd., Corvallis, OR 97330, USA

Abstract

The microstructures and mechanical properties of the 316L austenitic stainless steel fabricated using binder jet printing (BJP) and selective laser melting (SLM) were investigated and compared with those of the conventionally manufactured (CM) alloy, with particular emphasis on the unnotched fatigue resistance. Results show that the work hardening behavior, ductility, and fatigue strength (σ_f) of the BJP specimens, which contain significant amounts of pores, are surprisingly comparable to those of the CM alloy. In contrast, the SLM specimens are considerably stronger, especially in terms of the yield strength, less ductile, and far inferior in terms of σ_f although the porosity in them is relatively smaller as compared to the BJP specimens. These results are rationalized by recourse to the distinct microstructures in the two additively manufactured alloys, which stem from the different processing conditions experienced by them. The planar slip regime that prevails in the early stages of plastic deformation of the BJP alloys and a combination of other microstructural factors lead to the arrest of small cracks that nucleate at the corners of the pores, both under quasi-static and cyclic loads; as a result, neither ductility nor fatigue strength are adversely affected by the porosity in the BJP alloys. In the SLM alloy, the cellular structure, which enhances the yield strength considerably, is too fine whereas the columnar grains are minimally misoriented and coarse enough to induce any crack deflection or arrest. Implications of these results in terms of possible directions for designing AM alloys with high mechanical performance are discussed.

Keywords: Austenitic stainless steels; high cycle fatigue; fatigue crack initiation; porosity; binder jet printing.

* Corresponding author; email: uram@ntu.edu.sg

1. Introduction

Additive manufacturing (AM) of metallic components can be achieved using a number of different processing techniques that use powder, wire, and sheets as raw materials. The AM processes that use metal powder as the raw material are selective laser melting (SLM), electron beam melting (EBM), and binder jet printing (BJP) [1], all of which are known as powder bed processes. The SLM and EBM techniques use laser and electron beams, respectively, for melting the powder. Microstructures and mechanical properties of different alloy components fabricated using these two techniques are the most widely studied and reported. In contrast, the BJP process is relatively less explored and structure-property correlations in the metallic parts produced using it are not as widely reported. In this technique, a strong green part is first produced by applying the binding agents at desired locations [2–4]. The green part is then sintered in a furnace [5]. Although all the three aforementioned processes are powder based, the following are the key differences from the metallurgical perspective in them. (i) In the SLM and EBM processes, a small volume of powder is rapidly melted, which subsequently solidifies rapidly. This, in turn, imparts a fine microstructure that can be hierarchical in some alloys [6–8]. In most cases, the line-by-line, layer-by-layer building of components imparts a mesostructure that reflects it; such a structure could be beneficial for simultaneous enhancement of strength and fracture toughness in some instances, but may impart significant anisotropy to the mechanical behavior [9,10]. The microstructures of the BJP alloys, in contrast, are neither as fine nor exhibit mesoscopic features [11]. (ii) The rapid quenching inherent in SLM and EBM processes can result in the formation of metastable microstructural phases, though it is possible to avoid the formation of such phases by in-situ modifications, for example, raising the temperature of the powder bed. However, often the as-fabricated parts are unsuitable for high temperature applications and requires post processing [12,13]. Since the BJP parts require long sintering times, the resulting microstructures are relatively more stable. (iii) The larger thermal gradients and repeated heating and cooling of the deposited layers in the SLM processes can result in the presence of a high degree of residual stress in the fabricated coupons. As a result, they often require a post-fabrication annealing treatment to relieve those stresses. In contrast, the BJP specimens are almost free from any residual stresses [2,14].

The major advantage of the BJP process is its capability to produce parts relatively cheaply and comparatively faster via-á-vis other powder bed processes [15]. Importantly, it is amenable

to any kind of alloy, whereas AM using SLM/EBM techniques can only be performed on a handful alloys. It is also capable of printing ceramics and composites [16]. While porosity is inherent in all the parts manufactured using powder-based AM techniques, the porosity levels in the BJP alloys tend to be high (often greater than 1-2%). In contrast, SLM parts are printed routinely nowadays with relative densities higher than 99.5% [17,18]. The high porosity levels in the BJP alloys, which forms during the sintering of the consolidated green parts, is considered a major disadvantage, especially in structural applications that are prone to fatigue [2,14]. This aspect requires detailed examination, especially in view of the recent technological advances in terms of binding agents [2,4,5,19]. Keeping this in view, the microstructure, porosity, and their effect on the tensile and high cycle fatigue (HCF) behavior of a 316L grade austenitic stainless steel (SS), a widely studied alloy in the SLM context, were investigated in the present work. The obtained results are compared with those of 316L SS manufactured using SLM as well as conventional manufacturing (CM) processes. Although the porosity level in the SLM alloy is significantly low as compared to that in the BJP alloy, it was found that its HCF resistance is far inferior, whereas the fatigue strength of the BJP alloys is comparable to that reported for fully-dense CM alloy. We rationalize these surprising results by recourse to detailed studies on crack-microstructure interactions.

2. Materials and experiments

2.1. Materials

In this paper, we compare the mechanical properties of 316L SS specimens (with particular emphasis on unnotched fatigue) that were manufactured using three different processes: BJP, SLM, and CM. All the results on the BJP coupons presented in this work are new. While the unnotched fatigue test results on SLM specimens are new, results of the microstructural characterization, quasi-static tensile tests, fracture toughness and fatigue crack growth measurements on SLM 316L specimens that were fabricated using identical processing conditions were reported by some of us [6] in an earlier paper. For CM specimens, while quasi-static tensile tests were performed as a part of this study, fatigue data are taken from published literature.

For unnotched fatigue testing, cylindrical SLM specimens with a total length of 64 mm and a diameter of 9 mm were printed by Concept Laser Machine equipped with a YAG fibre laser.

The following process parameters were used for printing: laser power −90 W, scan speed −1000 mm/s, hatch spacing −150 µm (30% overlap), layer thickness −30 µm, scan rotation between the successive layers − 90°. The samples were printed with the hatch style known as single melt (SM), details of which have been reported elsewhere [6]. After printing, these specimens were stress relieved at 500 °C for one hour. While quasi-static tensile tests were performed in both P- and S-orientations (wherein the loading direction is parallel and perpendicular to the build direction, respectively), unnotched fatigue tests were performed on samples whose long axis coincides with the build direction, i.e., only in the P-orientation. We would like to point out that the parameter used for printing SLM 316L is not optimized, thus it contains relatively high degree of porosity.

Rectangular BJP specimens (length = 70 mm) with 10 mm by 10 mm square cross-section were manufactured using the HP Metal Jet technology, using 316L powder and water based liquid binding agent[1] [19]. The capillary forces pull the binding agent in the smallest interstices formed between the metal powder, which helps in uniform distribution of the binding agent [19]. After the printing of the parts, the curing of the bed evaporates the water of the binding agent and results in a strong green part. The green parts are then sintered in a furnace where the binding agent decomposes and fusion of the metal powder results in a solid part. The final stage of sintering was performed at temperature of 1380 ˚C for 120 minutes in a hydrogen atmosphere. The BJP specimens were printed in two different orientations, perpendicular and parallel to the direction of powder spreading. From now on we will refer them as P- and S-series, respectively.

The tensile CM specimens were machined from a commercially available hot rolled plate annealed at 1050 ˚C and air-cooled. The properties of the steel plates satisfy the criteria set by ASTM A240/A240M–17 for their use in pressure vessels or general applications [20].

2.2. Experiments

The relative density of all the specimens examined in this study were measured using the Archimedes' principle with an weighing scale El Analytical balance XS204 capable of measuring weight to 0.0001 g accuracy (which translates to 0.00125% relative density accuracy for the 316L SS [21]). Ethanol was used for the measurement instead of water because the

[1]*These samples were received early in the development of the HP Metal Jet process, where further optimization and improvement continues as the technology is commercialized.*

surface tension of ethanol is ~ 3 times lower than the water, which reduces the error in measurement of relative density [22]. All the specimens were mirror polished for the microstructural characterization by optical microscope (OM) and scanning electron microscope (SEM). The SLM specimens were etched after mirror polishing by V2A etchant (100 ml distilled water, 100 ml HCl, 10 ml HNO_3) so as to highlight the grain boundaries and other microstructural features. Compositional analysis of both BJP and SLM specimens was carried out by wavelength-dispersive spectroscopy (WDS) using electron probe micro-analyzer (EPMA). For elemental mapping by WDS, a step size of 0.5 µm was used in EPMA. Electron back-scattered diffraction (EBSD) with step size of 0.5 µm was used for phase and grain orientation mapping, which is represented in the form of inverse pole figure (IPF) maps. These IPF maps were also used to measure the grain size, *d*, of the BJP and CM specimens. Further, the solidification cell size (described later) in the SLM specimens was measured using ImageJ, an open source software.

While uniaxial tensile testing was performed on the 316L specimens manufactured using BJP, SLM and CM processes, fatigue testing was carried out only on BJP and SLM specimens. For uniaxial tensile testing of the BJP and CM specimens, flat dog bone shaped coupons were machined with the gauge length of 20 mm, width of 4.8 mm, and thickness of 3.3 mm. Respective dimensions of the tensile SLM specimens were 6, 2 and 0.5 mm. Following the standard procedures described in ASTM E8/E8M-11 [23], the tensile tests were conducted at a nominal strain rate of 10^{-3} s^{-1}. During the tests of BJP and CM specimens, the strain was monitored using a video extensometer; for the SLM specimens the strain was monitored using a laser extensometer due to their sub-size dimensions.

Since the relative porosity of both the P- and S-series BJP specimens varied significantly, tensile tests were carried out on the specimens with four different levels of porosity so as to evaluate the effect of porosity on the tensile properties. High cycle fatigue behaviour of SLM, BJP specimens of both P and S-series were evaluated in the rotating bending fatigue (RBF) configuration which operates at a constant frequency of 50 Hz. The unnotched fatigue testing was carried out on hour-glass shaped specimens with gauge length of 22 mm and a minimum diameter of ~5 mm machined out of square rod shaped printed parts, following the procedure described in the international standard, ISO-1143 [24]. To minimize the effect of surface roughness on the fatigue properties, all the specimens were polished till average surface

roughness, R_a was less than 1 µm. To determine the fatigue strength, σ_f, of SLM specimens, first sample was tested at stress amplitude, σ_a, of 300 MPa which is nearly half of the tensile strength, σ_u. Further, σ_a was reduced by 25 MPa till the σ_a reached a value at which at least three samples survive 10^7 cycles and the corresponding σ_a is designated as σ_f. However, in both P and S-series BJP specimens, the RBF tests were first started at a σ_a = 150 MPa and then increased by 50 MPa till a sample failed before 10^7 cycles. This approach was employed in anticipation of a low σ_f (because of comparatively high relative porosity in BJP specimens). However, the first sample to fail below 10^7 cycles was that subjected to σ_a = 300 MPa.

To further study the effect of porosity on fatigue behaviour with a reasonable statistical accuracy, a total of 17 samples from P and S-series with different porosity levels were tested at σ_a = 270 MPa. The runout specimens tested at 270 MPa were nickel plated, sectioned (using wire electrical discharge machining (EDM) so as to preserve the sections close to the surface) and then mirror polished to observe internal fatigue cracks, if any. Fractography using SEM was carried out on all the fractured specimens failed during to uniaxial tensile testing as well as RBF testing.

3. Results

3.1. Microstructures

An optical micrograph of a BJP specimen is displayed in Fig. 1a. It shows equiaxed grain structure that is typically observed in 316L SS after solution annealing treatment [25–27]. Both the P and S-series samples show similar microstructures in all the three orientations, which is expected as BJP process does not intrinsically favor (or aid) microstructural anisotropy, unlike SLM. A SEM micrograph of the BJP 316L SS, displayed in Fig 2a, shows presence of a second phase along some of the grain boundaries, which appears to be δ-ferrite formed during sintering process [28]. The presence of δ-ferrite was confirmed by WDS elemental maps shown in Figs. 3a, b and c; these images show the segregation of ferrite stabilizing elements Cr, Mo at these sites. The results of WDS compositional analyses of the ferrite phase and the matrix, listed in Table 1, show that while Ni concentration in the matrix is ~11 wt.%, it is only ~4.5 wt.% in the ferrite. An IPF map obtained using EBSD on BJP specimen is displayed in Fig. 4a. It shows equiaxed grains with a grain size (d) of ~26 ± 16 µm, whereas the phase map displayed in Fig. 4b indicates the presence of ~2.63% δ-ferrite in it. Both the images indicate to the presence of

significant amount of annealing twins. Misorientation mapping across the twin boundaries in Fig. 4b shows that they are <111> 60° type and constitute ~11.6% in terms of area fraction. These annealing twins are also present in CM specimen, see the IPF map displayed in Fig. 4c, amidst equiaxed grains of size, $d \sim 18 \pm 17$ µm.

An optical micrograph of the SLM specimen (on plane perpendicular to the build direction) in Fig. 1b shows grains elongated in the direction of the laser scanning tracks. Microstructure of the SLM specimen on the plane parallel to the build direction is displayed in Fig. 2b. It shows formation of melt pool boundaries, which make the microstructure anisotropic. The anisotropy in the microstructure and mechanical properties of SLM 316L manufactured using identical SLM parameters was reported in an earlier work by us, where the effect of micro-meso-structure on the tensile properties, fracture toughness, and fatigue crack growth behaviour was analysed [6]. Figs. 3d, e and f show the WDS maps obtained on the SLM specimen. They indicate a uniform distribution of all the elements, indicating the microstructure of SLM 316L specimens consists only of the austenite (γ) phase. Higher magnification image, displayed in the inset of Fig 2b, shows presence of fine solidification cellular structure with an average cell diameter of ~ 0.75±0.8 µm. Such fine cell structure is attributed to the high rate of cooling, which results in a steep thermal gradient in the molten metal [6,29]. Prior studies have also shown that both Cr and Mo segregate to the cell boundaries [7].

3.2. Porosity

Figures 5a and b show the distribution of pores in BJP and SLM specimens, respectively. In both the cases, the pores appear irregularly shaped. Their angularity, however, appears to be comparatively less, i.e., they are relatively more spherical in nature, in the BJP specimens than in SLM specimens. In the latter, the pores form across several layers of deposition, possibly due to an inadequate melt-pool overlap caused by the single melt (SM) deposition strategy [6].

The 3D porosity distribution in BJP specimens were further analysed using X-ray micro computed tomography (XRMCT). A representative image is shown in Fig. S1 of the supplementary information (SI). The pores that appear to be randomly distributed in optical micrographs are in fact aligned along the build direction when observed using XRMCT (see Fig. S1b of SI). Such an alignment of the pores is possibly related to the line by line deposition of the binder material ensuing a gradient in the compaction/green strength of the parts, which would

result in higher porosity in the less compact region during the sintering process.

The relative porosity in all the tested specimens were measured using the Archimedes principle. While relative porosity in SLM specimens is ~ 2.3%, which is consistent through all the SLM blocks, it varies from 3.86 to 5.59 % in P-series and 3.73 to 5.29% in S-series of the BJP specimens. Figures S2a and b of SI show the porosity variation in each of the BJP specimens examined in this study.

3.3. Tensile properties

To examine the effect of porosity on the stress-stress behaviour of BJP specimens, if any, four specimens from both P and S-series with different porosity levels were selected and tested. The measured tensile stress-strain responses are displayed in Fig. S3 of SI. Average values of the 0.2% yield strength (σ_y), σ_u, and elongation to failure (e_f) extracted from those responses are listed in Table 2. These results suggest that within the range of porosity examined in this study the tensile behavior remains unaffected. Additionally, it appears that the ductility of the alloy is substantial (ranging between ~64 to 81%), in spite of the relatively high porosity levels. The overall similarity between the tensile properties of P- and S-series specimens indicates that the BJP 316L SS are mechanically isotropic, reflecting the microstructural isotropy in the specimens examined in the present study.

The tensile stress-strain responses of the 316L specimens manufactured using SLM, CM and BJP techniques are compared in Fig. 6a and the property data is listed in Table 2. The following are some key observations. (i) σ_y of the SLM specimens is substantially larger than that of the BJP and CM specimens; in between the latter two, CM alloy exhibits ~35% higher σ_y. (ii) The disparity in σ_u is not as marked; while SLM (in P-direction) and CM specimens have similar σ_u, the strength of BJP specimens is only lower by ~11% (on average). (iii) The high strength of SLM alloy comes at the cost of ductility, with e_f of them being as low as 12% (in the S-direction), Surprisingly, e_f of the BJP alloys is either similar or in many cases better than that of the CM alloy, indicating the presence of the porosity does not adversely affect the ductility in the BJP alloy. Difference in the geometry of SLM and BJP specimens would affect the value of e_f, however, the difference in value of e_f is too high, thus, making the effect of geometry insignificant. (iv) Unlike the BJP specimens, the SLM ones show considerable anisotropy both in strength and ductility, with all the mechanical properties being significantly inferior in the direction perpendicular to build direction.

To examine whether the observed variations in σ_y across specimens manufactured using different processing techniques are due to the differences in the characteristic microstructural length scales (λ) that control the yield behavior of 316L SS, whose strength is known to be sensitive to the grain size [30], σ_y is plotted as a function of $\lambda^{-0.5}$ in Fig. 6b as per the well-known Hall-Petch relationship, i.e., $\sigma_y = \sigma_{fr} + K_y (\lambda)^{-0.5}$, where σ_{fr} is friction stress, K_y is locking parameter. Data reported on CM alloys with different grain sizes (d) is also used in this plot for comparison [6,25,31,32]. While $\lambda = d$ for the BJP and CM alloys, it is taken as the cell size in SLM alloys. A reasonably good fit through the data, with σ_{fr} = 188 ± 14 MPa and K_y = 275 ± 21 MPa.(μm)$^{0.5}$, observed in Fig. 6b suggests that the fine solidification cell structure in the SLM specimens is the reason behind the observed high σ_y in them. It has been reported that even though the cell walls in this case are dislocation cell wall in the 'conventional' sense, but are a result of the segregation of elements like Cr and Mo, which, in turn, necessitate that cell walls contain a high density of geometrically necessary dislocations (GNDs) [6,7].

From Fig. 6b, we note that the σ_y of BJP specimens is lower (by ~60 MPa or ~20%) than that of 316L SS with similar grain size predicted by the Hall-Petch relation. This reduction is possibly due to the relatively high porosity levels in these specimens, as pores can raise the stress locally and result in the onset of plastic deformation at lower stress levels [33,34]. Mil'man [35], Bocchini [36], and Klar et. al. [37] reported that σ_y of sintered ferrous alloys decreases with the porosity level according to the equation proposed by Ryshkevitch [38]: $\sigma_y = \sigma_{y,0} \times \exp(-6.5f)$, where $\sigma_{y,0}$ is the yield strength of fully dense alloy (taken as 260 MPa for 316L with d ~ 26 μm [39]) and f is the pore volume fraction. For the range of f observed in the BJP alloys examined in the present work (3.7 to 5.6%), the above relation predicts σ_y between 181 and 204 MPa, which is in good agreement with the experimentally measured range of 189 and 198 MPa (see Table 2).

3.4. Work hardening behavior

The tensile stress-strain responses displayed in Fig. 6a clearly indicate that the work hardening behavior of SLM 316L SS is significantly different from that of the BJP and CM alloys. While the latter two yield at relatively low stresses and then strain harden considerably before necking, the SLM alloy does not exhibit much work hardening, which is the reason for the relatively low ductility in it. To explore these characteristics further, stress-strain data in the plastic regime of all the three alloys is displayed in Fig. 7a on a log-log plot. Both the BJP and CM specimens

exhibit the characteristic two stage hardening that is widely reported to occur in well-annealed 316L SS [40]; the following are the mechanisms behind [40,41]. Beyond yield, easy and planar glide of dislocations leads to the observed initial low hardening rate [42]. However, when the dislocation density increases with the plastic strain, an enhanced resistance to their mobility leads to cross-slip, leading eventually to the formation of dislocation cells. This transition in the mechanism causes the secondary steady state hardening with a considerably higher hardening rate [40,41].

The two stage hardening behaviour can be well-described by the Ludwigson's constitutive relationship [40]:

$$\sigma = K_1 \varepsilon_p^{n_1} + \exp^{K_2} . \exp^{n_2 \varepsilon_p} \quad (1)$$

where σ is the true stress, ε_p is the true plastic strain, K_1 and K_2 are material constants known as strength factors, and n_1 and n_2 are the work hardening indices. Fig. 7b shows representative experimental data (in the plastic regime) obtained on the P- and S-series BJP and CM specimens, with Eq. (1) fitted through them. The values of K_1, K_2, n_1, and n_2 for BJP and CM specimens obtained through such fits are listed in Table 3 along with those reported in literature for a CM 316L that has similar d (~26 µm) as the BJP alloys examined in this study [42].

The values K_1 and n_1 represent the slope of the second stage of hardening shown in Fig. 7a, where cross slip is prevalent. The BJP specimens show higher n_1 as compared to the CM specimens, which could be related to different microstructure of BJP and CM specimens. The value of n_1 reported by Singh et. al. [42] for 316L SS with a similar d, but manufactured using the CM techniques, is also lower than that estimated for BJP specimens. Singh et al. emphasized that when d > 6 µm, d has a negligible effect on n_1. Since d in the BJP alloys is much larger than this critical size, it might not be the reason for the observed differences. The other two remaining factors that can affect the hardening behavior are the stacking fault energy (SFE) and presence of δ-ferrite. The mechanism of plastic deformation in austenitic SS transitions from deformation twinning when SFE is ~15-45 mJ/m^2 to dislocation glide when SFE ≥ 45 mJ/m^2 [43]. An approximate estimate of the SFE, on the basis of the chemical compositions given in Table 1 and using the JMatPro software, yields a value of ~ 48.1 mJ/m^2 for the matrix of the BJP alloy due to segregation of Cr, Mo and depletion of Ni at the grain boundaries (which result in the formation

of δ-ferrite, as discussed earlier), whereas it is ~ 56.2 mJ/m^2 for the SLM alloy in which all the elements are uniformly distributed. Although the SFE in the BJP specimens is relatively lower, the predominant deformation mechanism is still dislocation glide due to the fact that it is greater than 45 mJ/m^2. However, the relatively lower SFE can prolong the 'easy glide' stage of plastic deformation, which will be discussed later.

The presence of δ-ferrite in the BJP alloys can directly affect the hardening behavior as well. Although the crystal structures of δ-ferrite (BCC) and γ-austenite (FCC) are different, the Kurdjomov-Sachs orientation relationship, $[110](1\bar{1}1)_\gamma//[111](1\bar{1}0)_\delta$, between them facilitates slip transfer [44]. However, δ-ferrite is considerably harder due to the absence of closed pack planes in the BCC crystal structure, which leads to strain incompatibility between the two phases. (See Fig. S4 of SI that shows the hardness values of the two phases evaluated using the nanoindentation technique.) While the austenite phase deforms readily, slip transfer through the ferrite phases starts only at a larger strain [44]. Thus, the presence of ~2.63% δ-ferrite is the possible reason along with the extended planer glide for the observed higher n_1 in the BJP specimens compared to CM specimens.

The two stage hardening in the BJP specimens resulted in a σ_u to σ_y ratio of ~3, which, in contrast, is merely 1.2 in the case of SLM specimens. This difference also reflects in elongation to failure, e_f which is ~3.5 times higher in BJP specimens as compared to that in the SLM specimens.

Representative fractographs obtained from the tensile tested BJP and SLM specimens are displayed in Figs. 8a and b, respectively. While the BJP specimens show ductile dimple fracture features, they are less prevalent in the SLM specimens. (See Fig. S5 in SI for the low magnification images of the fractured samples.) The ductile dimples in the BJP specimens are reminiscent of the porosity distribution observed using XRMCT (See Fig. S1 of SI), which suggests that the void coalescence and growth is aided by the existing pores.

3.5. Fatigue strength

Results of the RBF tests on the BJP (P-series) and SLM (P-orientation) specimens are displayed in Fig. 9. (See Fig. S6 in SI for the fatigue data on the S-series of the BJP alloy.) The σ_f of SLM specimen is considerably low at 101 MPa, which only about one-sixth of σ_u. One possible explanation for this is the high relative porosity ~ 2.3% in them. For example, from a

series of tests conducted for up to a million cycles, Solberg et al. [43] reported σ_f ~ 163 MPa. The presence of large 'lack-of-fusion' pores were the reason for such a low σ_f. Chefan et al. [45] suggested that eliminating such pores can improve σ_f to ~ 200 MPa. Elangeswaran et al. [46] and Riemer et al. [47] demonstrated that σ_f of SLM 316L can be improved to ~250 MPa by reducing the porosity level below 0.5%. Surprisingly, σ_f of both P- and S-series BJP 316L SS is ~250 MPa, in spite of the fact that the relative porosity in them is considerably higher, ranging between 3.7% and 5.6%, i.e., almost 2 to 3 times higher compared to that in the SLM specimens.

To assess the effect of porosity on the fatigue behavior, 17 samples from both P and S series with the entire range of porosity variation were tested at σ_a, 270 MPa. The relative porosity vs. number of cycles to failure (N_f) data obtained on these specimens is displayed in Fig. 9c. It shows that 12 out of the 17 samples survived 10^7 cycles. Importantly, we did not find any correlation between the porosity and N_f of those specimens which failed earlier than 10^7 cycles, suggesting that the porosity has no apparent effect on the fatigue behavior of the BJP specimens within the range of porosity investigated.

A comparison of the σ_f of the AM specimens with those of CM specimens is essential for bench-marking purposes. A survey of the published literature on the RBF test results on CM specimens indicates a large variance in the reported σ_f, which is possibly due to the large variation in the microstructures and thermal histories of the alloy samples examined. In view of this, we compare σ_f of BJP specimens with that of a well-annealed 316L whose σ_u is of similar to that of the BJP specimens. In such cases, reported data of σ_f of CM 316L range between 250-350 MPa, and σ_f /σ_u ratio ranges between 0.40 to 0.49 [46–49]. While σ_f (250 MPa) of the BJP specimens investigated in this work is at the lower end of this range, the σ_f /σ_u ratio (~ 0.45) can be considered impressive considering the level of porosity in them.

Representative low magnification fractographs of the fatigue tested (σ_a = 300 MPa) BJP and SLM specimens are displayed in Figs. 10a and b, respectively. The fracture surface of the BJP specimen is highly corrugated as compared to that of the SLM specimen; possibly because of relatively high ductility of BJP specimens. The crack initiation sites can be easily identified in both the cases; these locations are marked with red boxes. Higher magnification images of these regions are provided in Figs. 10c and d. They show that the crack initiates from a pore (which appears to have formed due to an unmelted powder particle) close to the specimen surface of the SLM sample. In the case of the BJP specimen, no pores were detected at the crack initiation site.

Instead, the fatigue crack appears to initiate from the surface. Similar observations were made in almost all the BJP and SLM specimens.

4. Discussion

4.1. Effect of hardening behaviour on the fatigue crack initiation

A large fraction of the HCF life of any material is spent in initiating the dominant crack that eventually lead to failure [50]. Since the presence of pores, especially close to the surface, makes it considerably more easy to initiate a sharp crack under cyclic loading conditions, the HCF life of materials with porosity tend to be far inferior as compared to their pore-free counterparts. This is precisely the reason for the observed σ_f of 101 MPa in the SLM specimens of the current study. (In fact, this is the major drawback of almost all the AM metals that are fabricated used either SLM or e-beam melting techniques.) In the case of the BJP specimens, although the porosity level in them is considerably higher than that in the SLM specimens, σ_f is ~ 250 MPa, which is close to the value of CM 316L [46–49,51]. It is also interesting to note that this σ_f is larger than the σ_y of the BJP alloys.

Fatigue crack initiation in a material depends on a number of factors and an important one is how dislocations interact with microstructural elements such as grain boundaries, inclusions, and pores [52]. Since the strain hardening behaviors of the BJP, SLM and CM specimens--and hence ductility--differ significantly, it is possible that this could be the reason behind the observed difference. In particular, the interaction between the planer slip, which is prevalent in the early stages of plastic deformation in BJP and CM alloys, and the pores during fatigue loading could shed some light on the underlying reasons. It has been observed that when planer slip is prevalent, small cracks tend to grow along the slip planes. This, in turn, can lead to the a reduction in the mode-I driving force when the slip plane is inclined to the loading axis [53,54]. In the SLM specimens, planar slip does not occur because of the fine cellular structure in it promotes the dislocations to cross-slip at the onset of plastic deformation itself [7].

Plastic deformation in the BJP and the CM specimens, however, exhibits the initial easy glide stage, which transitions into duplex slip that facilitates eventual cross-slip. To demarcate the stress/strain at which this transition starts to occur, the work hardening rate, $d\sigma/d\varepsilon$ is plotted as a function of the true strain, ε, in Fig. 11. The true transition strains, ε_T, at which flow transition from planar to duplex slip occurs (designated by TP_1 and TP_2 for the CM and BJP

specimens, respectively) are identified by recourse the tangent-intersection method as illustrated in Fig. 11. The corresponding engineering stresses are labeled S_T. The average values of ε_T and S_T for the BJP specimens are ~ 2.37 ± 0.3%, and 253 ± 13 MPa, whereas they are 1.57% and 359 MPa for the CM specimens. This indicates that the planar slip regime is prolonged in the BJP specimens, which could be due to the lower SFE in them, as discussed already in section 3.3.

To understand the role of higher ε_T in BJP specimens and how the planer slip affects crack initiation, interrupted tensile tests on the BJP specimens were carried out. As illustrated in Fig. 12a, the tests were interrupted for the microstructural evaluation by SEM at S = 200, 220, 250, 270, and 400 MPa, which correspond to e of 0.11, 0.41, 1.36, 2.14, and 11.6%, respectively. Only planer slip could be noted until e = 1.36% (S = 250 MPa); see Fig. 12b. Upon further straining (e = 2.14% and S = 270 MPa), microcracks starts to form around the pores, as illustrated in Fig. 12c. Note that these stress levels correspond to those of the transition stresses, S_T. The orientation of these cracks appears to broadly align with the slip lines. When S is further increased to 400 MPa (e = 11.6%), duplex slip becomes prevalent, which first starts near the pores due to high stress concentration, as illustrated in Fig. 12d. The duplex slip lines form at an obtuse angle to the planer slip lines, because of which, the cracks that had formed near the pores along the direction of the planar glide are not aligned with the slip lines. As a result of this, any cracks that nucleate at the pore corners get arrested. This is possibly the reason as to why porosity does not affect the ductility of the BJP specimens in an adverse manner.

It appears that the duplex slip first starts in the grains that contain pores. To illustrate this, one BJP specimen, whose surface was carefully made ready for EBSD, was strained to e = 4% (S = 300 MPa). While Figs. 13a and 13b show low magnification SEM micrographs obtained before and after the tensile test, Figs. 13c and 13d show the Kernel Average Misorientation (KAM) maps obtained from the locations I and II marked on images 13a and 13b, respectively. Localisation of plastic strain near the pores and the grain boundaries can be seen in Fig. 13d. SEM images of this sample before and after loading are displayed in Fig. S7 of SI, so as to further illustrate crack blunting by the process of duplex slip.

4.2. Small fatigue crack growth

From Fig. 12c, it is apparent that microcracks start forming in the BJP specimens in the stress range of 250-270 MPa under quasi-static tensile loading. Most of these cracks get blunted due to

the initiation of the duplex slip. Under cyclic loading, only one crack has to attain the critical length for it to cause early failure. Yet, 12 out of 17 specimens tested at σ_a = 270 MPa 'ran out', indicating a high degree of damage tolerance intrinsic to the BJP specimens. To contrast, all SLM specimens subjected to fatigue testing at $\sigma_a \geq 200$ MPa did not even survive 500,000 cycles. Fractographic investigation of these specimens indicates that the cracks originate from the lack-of-fusion pores, whose diameter, η, is in the range of~ 300-400 µm. From linear elastic fracture mechanics (LEFM), the critical flaw size, a_c, below which a crack does not propagate can be determined on the basis of the threshold stress intensity factor range for large crack, ΔK_{th}^{LC} [55,56] as,

$$a_c = \frac{1}{\pi}\left(\frac{\Delta K_{th}^{LC}}{Y.\sigma_a}\right)^2 \quad (2)$$

where, Y is the shape factor (~1.1 [56]). Using the value of 9.1 MPa$\sqrt{m}$ for ΔK_{th}^{LC} that was reported by us for this specific SLM 316L [6] and σ_a = 200 MPa in Eqn. (2) gives a_c = 545 µm, which is much larger than the η of the pores that cause the failure of these specimens. This observation implies that the cracks that nucleate at the pore corners have to grow by at least 150 µm, before they become critical. As we shall see later, the microstructure in the SLM alloy does not provide any hindrance for such growth.

To investigate the reasons for the excellent fatigue resistance observed in the BJP specimens, microstructural evaluation on the surfaces as well as cross-sections of the runout specimens tested at σ_a = 270 MPa was performed. Three representative images of small fatigue cracks (SFC), which emanate from pores but get arrested (inferred, as the specimens ran out), and their interaction with the microstructural constituents are displayed in Fig. 14. Although one of these cracks has propagated a distance of ~ 40 µm (Fig. 14c), the specimen survived 10^7 cycles. Such crack arrest has been observed in the past, especially in the materials where planar glide is prevalent wherein the SFCs can maintain their crystallographic nature until they propagate over tens of grains; crack growth along the slip bands is often limited to only one or two grains in materials with wavy slip characteristics [53,57].

The fracture surface of a BJP specimen tested at σ_a, 300 MPa, displayed in Fig. 10c, indicates that a small crack initiated from a pore near the surface of the specimen and grew along

the circumference for about 500 µm before it started to grow inwards. While the growth of such SFCs can sometimes be faster than the large fatigue cracks, they can be hindered by microstructural features such as large angle grain boundaries or when they encounter a different microstructural phase along its path [58,59]. The propagation of a SFC through a grain boundary can occur through the accumulation of sufficient damage in the adjacent grain. However, direct transfer of slip (and hence crack propagation) is not possible under HCF conditions as the σ_a is relatively small [57,58,60].

The ability of the grain boundaries to resist the growth of a SFC depends on the following factors. (i) Grain size, d which controls the size of the blocked slip bands. (ii) The relative orientation of the grains with respect to the direction of loading, which determines the ratio of Mode I and Mode II components of the crack driving forces. (iii) Misorientation between the grains. In order to predict the threshold stress amplitude, σ_{th}, that is required to grow a crack through the grain boundary, Tanaka et. al. [61] proposed the blocked slip band (BSB) model that estimates the size of the slip band required for transferring the damage through the grain boundary, which is a conceptually similar to that used in developing the Hall-Petch relationship [61–63]. According to the BSB model, the threshold stress intensity factor ranges for the propagation of large crack and small cracks, $\Delta K_{\mathrm{th}}^{\mathrm{LC}}$ and $\Delta K_{\mathrm{th}}^{\mathrm{SC}}$ respectively, are related through the equation [59]:

$$\Delta K_{\mathrm{th}}^{\mathrm{SC}} = \Delta K_{\mathrm{th}}^{\mathrm{LC}} \sqrt{\frac{a}{a+a_0}} + 2\,\sigma_{\mathrm{fr}} \sqrt{\frac{a}{\pi}}\, \cos^{-1}\left(\frac{a}{a+a_0}\right), \tag{3}$$

where a is half crack length, σ_{fr} is friction stress (~ 188 MPa, obtained from Fig. 6b), and a_0 is the length of the blocked slip band. An assumption that the stress concentration near the crack tip is higher than the microscopic yield strength of the grain through which the crack has to break through gives [52,59]:

$$a_0 = \left(\frac{d}{2}\right)\left[\frac{\sigma_{\mathrm{a}}}{\alpha M \sigma_{\mathrm{f}}}\right]. \tag{4}$$

Here, α is a constant (=0.6 for 316L [64]) and M is the Taylor factor, which is taken as the minimum value obtained from the IPF maps (=2.3). From literature [6,65], values of 7.9 and 13.5

MPa$\sqrt{\text{m}}$ were used for $\Delta K_{\text{th}}^{\text{LC}}$ for the BJP (well-annealed 316L SS with similar grain size as the BJP specimens) and the SLM specimens, respectively; both the values are corrected for load ratio, $R = -1$. An important point to note here is that a_0 depends on the applied σ_a. The above model also includes the effect of mode II component of the crack growth, which usually is the case for small cracks. Once $\Delta K_{\text{th}}^{\text{SC}}$ is determined using Eqns. (3) and (4), σ_{th} can be evaluated using the following fracture mechanics equation [59]:

$$\sigma_{\text{th}} = \frac{\Delta K_{\text{th}}^{\text{SC}}}{\sqrt{\pi a}}. \quad (5)$$

Variations of σ_{th} in both the BJP and SLM specimens for σ_a = 250 and 300 MPa are plotted as a function of the crack length a in Fig. 15. Following are some observations. (i) The value of σ_{th} for growth of a SFC across a grain boundary in a BJP specimen is ~ 700 MPa for a crack length of 40 µm. Since the applied stress is much smaller than this stress, the crack gets arrested at the grain boundary. This is the reason why the samples survived 10^7 cycles even though it had a 40 µm long crack. This observation implies that the high σ_{th} translated into high σ_f in the BJP specimens. (ii) At σ_a = 300 MPa, σ_{th} of BJP specimen is nearly three times that of the SLM specimens. The reason behind such big difference is the d ~ 75 µm in SLM specimens compared to d ~ 26 µm in BJP specimens. The cellular structure in the SLM specimens, which is the reason behind their high strength, cannot hinder the growth of SFCs, because the misorientation between the cells is less than 2°. If the misorientation between two grain is < 15°, then the grain boundary is not an effective barrier to the SFC growth [58,60]. (iii) For σ_a of 300 MPa, σ_{th} is close to 400 MPa, which means that once a crack initiates from a pore, it will fracture very fast. This reflects in the fatigue results of the SLM specimen which failed in ~2×10^5 cycles when fatigued at σ_a = 300 MPa. Furthermore, the presence of large lack-of-fusion pores makes the initiation of such fatal cracks easy. (iv) When a is > 70 µm, σ_{th} of SLM specimen is higher compared to BJP. This observation suggests that the growth rate for a large crack is higher in BJP specimens compared to SLM specimens. Indeed the model is able to capture the effect of grain size on the growth of small and large cracks, as suggested in literature [52,59,66].

From the above discussion, the following reasons behind the superior unnotched fatigue resistance of the 316L SS BJP specimens, as compared to the SLM specimens, can be inferred.

(i) It is difficult to initiate a long fatigue crack in the BJP specimens because planar/duplex slip is primary deformation mechanism in low strain range. In the SLM specimens, in contrast, plastic deformation is aided readily through dislocation cross-slip because of the presence of fine solidification cellular structure. (ii) The microstructures of the BJP specimens contain an abundance of effective barriers, such as the annealing twin boundaries with a misorientation of 60°, δ-ferrite phases, and large angle grain boundaries, all of which hinder the growth of SFCs. (iii) In the SLM specimens, the sizes of the pores are relatively much larger. Moreover, they are not uniformly distributed, whereas pores are smaller and uniformly distributed in BJP specimens. Importantly, the microstructural length scales are either too large (columnar grains that are ~ 75 μm in size) or too small (cell size of 750 nm). Under such circumstances, a crack that readily nucleates at the corner of a pore, can traverse a substantial distance before it encounters a grain boundary. Since the crack considered long by that time, the effectiveness of the grain boundary as a barrier is lost, because the growth of the crack is not crystallographic anymore. Since the misorientation in 50% of columnar grain boundaries in the SLM specimens is < 5°, they are also less effective in arresting the growth of the fatigue cracks.

5. Conclusions and implications

On the basis of the experimental results obtained in this study, the following are some of the key conclusions that can be drawn.

(i) The substantial work hardening ability of both the BJP and CM 316L SS imparts them with considerable ductility. While the fine solidification cell structure within the columnar grains of the SLM alloy renders high yield strength to them, it forces dislocation cross-slip at the onset of the plastic deformation itself, shortening the work hardening regime, and hence ductility, in turn.

(ii) The planar slip deformation mechanism that governs the first stage of the plastic deformation in the BJP alloys coupled with high angle grain boundaries, δ-ferrite phase, and annealing twin boundaries, make it difficult for the cracks that nucleate at the pore corners during cyclic loading to grow to the required lengths for them to become critical. As a result the fatigue cracks remain short and crystallographic in nature and get arrested when they encounter these microstructural obstacles, when the applied stress amplitude is below the fatigue strength. In the SLM alloys, in contrast, the cell size is too small to act as a barrier for a crack to penetrate through (even at low stress amplitudes) whereas the columnar grains are too large and are well aligned to act as crack

arresters. As a result, fatigue cracks that nucleate at the pores near the surface of the specimen propagate unhindered, resulting in low fatigue resistance of the SLM alloy.

The following are the implications of the findings of the present work, in terms of possible directions for designing the AM 316L alloys with high mechanical performance, the following: While the higher porosity in the BJP specimens does not adversely affect its HCF resistance, it lowers σ_y. Thus, reducing the porosity substantially may make σ_y of the BJP parts as good as those of the CM alloy. For the SLM 316L SS, it is obvious that the occurrence of the lack-of-fusion pores should be minimized--if not eliminated altogether, so as reduce the overall porosity, and, in turn, enhance the fatigue strength. Microstructural design that would break the long columnar grains into smaller and equiaxed grains, may also make it more defect tolerant. In this direction, recent work that the crystallographic texture of 316L SS manufactured by SLM can be controlled by manipulating the melt-pool geometry and the solidification behavior [67,68] holds promise. Since the fine solidification cellular structure, which imparts the high yield strength to the SLM alloys, is reported to be thermally stable, heat treatments that would impart damage tolerance without compromising on the high strength in a significant manner should also be explored.

Acknowledgements

Part of this research was conducted in collaboration with HP Inc. and was supported by National Research Foundation (NRF) Singapore and the Singapore Government through the Industry Alignment Fund -Industry Collaboration Projects Grant (I1801E0028). The authors acknowledge the support of the HP-NTU digital manufacturing lab at NTU. UR acknowledges funding for 'Structural Metals and Alloys Programme' under RIE-2020 from A*STAR, Singapore. The authors thank Mr. Kashan Wimalasire of Nanyang Technological University (NTU) for his help with some of the experimental work.

References

[1] L.E. Murr, A metallographic review of 3D printing/additive manufacturing of metal and alloy products and components, Metallogr. Microstruct. Anal. 7 (2018) 103–132. doi:10.1007/s13632-018-0433-6.

[2] T. Do, P. Kwon, C.S. Shin, Process development toward full-density stainless steel parts with binder jetting printing, Int. J. Mach. Tools Manuf. 121 (2017) 50–60. doi:10.1016/j.ijmachtools.2017.04.006.

[3] A. Mostafaei, P. Rodriguez De Vecchis, I. Nettleship, M. Chmielus, Effect of powder size distribution on densification and microstructural evolution of binder-jet 3D-printed alloy 625, Mater. Des. 162 (2019) 375–383. doi:10.1016/j.matdes.2018.11.051.

[4] A. Mostafaei, A.M. Elliott, J.E. Barnes, C.L. Cramer, P. Nandwana, M. Chmielus, Binder

jet 3D printing – process parameters, materials, properties, and challenges, Prog. Mater. Sci. (2020) 100684. doi:10.1016/j.pmatsci.2020.100684.
[5] S. Mirzababaei, S. Pasebani, A review on binder jet additive manufacturing of 316L stainless steel, J. Manuf. Mater. Process. 3 (2019) 82. doi:10.3390/jmmp3030082.
[6] J. Suryawanshi, K.G. Prashanth, U. Ramamurty, Mechanical behavior of selective laser melted 316L stainless steel, Mater. Sci. Eng. A. 696 (2017) 113–121. doi:10.1016/j.msea.2017.04.058.
[7] Y.M. Wang, T. Voisin, J.T. McKeown, J. Ye, N.P. Calta, Z. Li, Z. Zeng, Y. Zhang, W. Chen, T.T. Roehling, R.T. Ott, M.K. Santala, P.J. Depond, M.J. Matthews, A. V Hamza, T. Zhu, Additively manufactured hierarchical stainless steels with high strength and ductility, Nat. Mater. 17 (2018) 63–71. doi:10.1038/nmat5021.
[8] J. Suryawanshi, K.G. Prashanth, U. Ramamurty, Tensile, fracture, and fatigue crack growth properties of a 3D printed maraging steel through selective laser melting, J. Alloys Compd. 725 (2017) 355–364. doi:10.1016/j.jallcom.2017.07.177.
[9] J. Suryawanshi, K.G. Prashanth, S. Scudino, J. Eckert, O. Prakash, U. Ramamurty, Simultaneous enhancements of strength and toughness in an Al-12Si alloy synthesized using selective laser melting, Acta Mater. (2016). doi:10.1016/j.actamat.2016.06.009.
[10] P. Kumar, O. Prakash, U. Ramamurty, Micro-and meso-structures and their influence on mechanical properties of selectively laser melted Ti-6Al-4V, Acta Mater. 154 (2018) 246–260. doi:10.1016/j.actamat.2018.05.044.
[11] M. Nastac, R. Lucas, A. Klein, Microstructure and mechanical properties comparision of 316L parts produced by different additive manufacturing process, in: Proc. 28th Annu. Int. Solid Free. Fabr. Symp., 2017: pp. 332–341.
[12] P. Kumar, U. Ramamurty, Microstructural optimization through heat treatment for enhancing the fracture toughness and fatigue crack growth resistance of selective laser melted Ti–6Al–4V alloy, Acta Mater. 169 (2019) 45–59. doi:10.1016/j.actamat.2019.03.003.
[13] P. Agrawal, S. Thapliyal, S.S. Nene, R.S. Mishra, B.A. McWilliams, K.C. Cho, Excellent strength-ductility synergy in metastable high entropy alloy by laser powder bed additive manufacturing, Addit. Manuf. 32 (2020) 101098. doi:10.1016/j.addma.2020.101098.
[14] P.K. Gokuldoss, S. Kolla, J. Eckert, Additive manufacturing processes: Selective laser melting, electron beam melting and binder jetting-selection guidelines, Materials (Basel). 10 (2017). doi:10.3390/ma10060672.
[15] H. Miyanaji, N. Momenzadeh, L. Yang, Effect of printing speed on quality of printed parts in Binder Jetting Process, Addit. Manuf. 20 (2018) 1–10. doi:10.1016/j.addma.2017.12.008.
[16] D. Suranga, D. Uduwage, Binder jet additive manufacturing of stainless steel-hydroxyapatite bio-composite, Minnesota State University, Mankato, 2015. http://cornerstone.lib.mnsu.edu/etds (accessed September 6, 2019).
[17] I. Gibson, D. Rosen, B. Stucker, Additive manufacturing technologies, Springer New York, New York, NY, 2015. doi:10.1007/978-1-4939-2113-3.
[18] F. Dini, S.A. Ghaffari, J. Jafar, R. Hamidreza, S. Marjan, A review of binder jet process parameters; powder, binder, printing and sintering condition, Met. Powder Rep. 75 (2020) 95–100. doi:10.1016/j.mprp.2019.05.001.
[19] HP, HP metal jet technology, (2018) 1–8. https://www8.hp.com/h20195/v2/GetPDF.aspx/4AA7-3333EEW.pdf.

[20] American Society for Testing and Materials, ASTM A240: Standard specification for chromium and chromium-nickel stainless steel plate , sheet , and strip for pressure vessels and for general applications, 2004. doi:10.1520/A0240.
[21] A.B. Spierings, M. Schneider, R. Eggenberger, Comparison of density measurement techniques for additive manufactured metallic parts, Rapid Prototyp. J. 17 (2011) 380–386. doi:10.1108/13552541111156504.
[22] G. Vázquez, E. Alvarez, J.M. Navaza, Surface tension of alcohol + water from 20 to 50 °C, J. Chem. Eng. Data. 40 (1995) 611–614. https://pubs.acs.org/sharingguidelines (accessed April 8, 2020).
[23] ASTM E8, ASTM E8/E8M standard test methods for tension testing of metallic materials 1, Annu. B. ASTM Stand. 4. (2010) 1–27. doi:10.1520/E0008.
[24] International Standard, ISO-1143 Metallic materials-Rotating bar bending fatigue testing, ISO 11432010(E). 2010 (2010) 1–6.
[25] D.M. Xu, G.Q. Li, X.L. Wan, R.L. Xiong, G. Xu, K.M. Wu, M.C. Somani, R.D.K. Misra, Deformation behavior of high yield strength – High ductility ultrafine-grained 316LN austenitic stainless steel, Mater. Sci. Eng. A. (2017). doi:10.1016/j.msea.2017.02.009.
[26] B.R. Kumar, S. Sharma, B. Mahato, Formation of ultrafine grained microstructure in the austenitic stainless steel and its impact on tensile properties, Mater. Sci. Eng. A. 528 (2011) 2209–2216. doi:10.1016/j.msea.2010.11.034.
[27] S.J. Wang, T. Jozaghi, I. Karaman, R. Arroyave, Y.I. Chumlyakov, Hierarchical evolution and thermal stability of microstructure with deformation twins in 316 stainless steel, Mater. Sci. Eng. A. (2017). doi:10.1016/j.msea.2017.03.073.
[28] P. V. Muterlle, M. Zendron, M. Perina, A. Molinari, Influence of delta ferrite on mechanical properties of stainless steel produced by MIM, in: 20th Int. Congr. Mech. Eng., 2009.
[29] K.G. Prashanth, J. Eckert, Formation of metastable cellular microstructures in selective laser melted alloys, J. Alloys Compd. 707 (2017) 27–34. doi:10.1016/j.jallcom.2016.12.209.
[30] S. Kheiri, H. Mirzadeh, M. Naghizadeh, Tailoring the microstructure and mechanical properties of AISI 316L austenitic stainless steel via cold rolling and reversion annealing, Mater. Sci. Eng. A. 759 (2019) 90–96. doi:10.1016/j.msea.2019.05.028.
[31] S. Ren-bo, X. Jian-ying, H. Dong-po, Characteristics of mechanical properties and microstructure for 316L austenitic stainless steel, J. Iron Steel Res. Int. 18 (2011) 53–59.
[32] A.J. Cooper, W.J. Brayshaw, A.H. Sherry, Tensile fracture behavior of 316L austenitic stainless steel manufactured by hot isostatic pressing, Metall. Mater. Trans. A. 49 (2018) 1579–1591. doi:10.1007/s11661-018-4518-2.
[33] N. Kurgan, Effect of porosity and density on the mechanical and microstructural properties of sintered 316L stainless steel implant materials, Mater. Des. 55 (2014) 235–241. doi:10.1016/j.matdes.2013.09.058.
[34] A. Gigovic-Gekic, M. Oruc, S. Muhamedagic, Effect of the delta-ferrite content on the tensile properties in nitronic 60 steel at room temperature and 750 °C, Mater. Technol. 46 (2012) 519–526. doi:669.14.018.8:669.112:620.17.
[35] Y. V. Mil'man, The mechanical properties of sintered materials. I. The strength properties of sintered materials, Sov. Powder Metall. Met. Ceram. 30 (1991) 30–39. doi:10.1007/BF00793397.
[36] G.F. Bocchini, The influences of porosity on the characteristics of sintered materials, SAE

Tech. Pap. 95 (1986) 790–805. doi:10.4271/860148.
[37] E. Klar, P.K. Samal, Powder metallurgy stainless steels: processing, microstructure, and properties, in: Powder Metall., 2007: p. 227. doi:10.1361/pmss2007p001.
[38] E. Ryshekewitch, Compression strength of porous sintered alumina and zirconia, J. Am. Ceram. Soc. 36 (1953) 65–68. doi:10.1111/j.1151-2916.1953.tb12837.x.
[39] K.K. Singh, S. Sangal, G.S. Murty, Hall–Petch behaviour of 316L austenitic stainless steel at room temperature, Mater. Sci. Technol. 18 (2002) 165–172. doi:10.1179/026708301125000384.
[40] D.C. Ludwigson, Modified stress-strain relation for FCC metals and alloys, Metall. Trans. 2 (1971) 2825–2828. doi:10.1007/BF02813258.
[41] S. Hertelé, W. De Waele, R. Denys, A generic stressstrain model for metallic materials with two-stage strain hardening behaviour, Int. J. Non. Linear. Mech. 46 (2011) 519–531. doi:10.1016/j.ijnonlinmec.2010.12.004.
[42] K.K. Singh, Strain hardening behaviour of 316L austenitic stainless steel, Mater. Sci. Technol. 20 (2004) 1134–1142. doi:10.1179/026708304225022089.
[43] D. Molnár, X. Sun, S. Lu, W. Li, G. Engberg, L. Vitos, Effect of temperature on the stacking fault energy and deformation behaviour in 316L austenitic stainless steel, Mater. Sci. Eng. A. 759 (2019) 490–497. doi:10.1016/j.msea.2019.05.079.
[44] C. Örnek, D.L. Engelberg, An experimental investigation into strain and stress partitioning of duplex stainless steel using digital image correlation, X-ray diffraction and scanning Kelvin probe force microscopy, J. Strain Anal. Eng. Des. 51 (2016) 207–219. doi:10.1177/0309324716631669.
[45] C. Yu, Y. Zhong, P. Zhang, Z. Zhang, C. Zhao, Z. Zhang, Z. Shen, W. Liu, Effect of build direction on fatigue performance of L-PBF 316L stainless steel, Acta Metall. Sin. (English Lett. 33 (2020) 539–550. doi:10.1007/s40195-019-00983-3.
[46] C. Elangeswaran, A. Cutolo, G.K. Muralidharan, C. de Formanoir, F. Berto, K. Vanmeensel, B. Van Hooreweder, Effect of post-treatments on the fatigue behaviour of 316L stainless steel manufactured by laser powder bed fusion, Int. J. Fatigue. 123 (2019) 31–39. doi:10.1016/j.ijfatigue.2019.01.013.
[47] A. Riemer, S. Leuders, M. Thöne, H.A. Richard, T. Tröster, T. Niendorf, On the fatigue crack growth behavior in 316L stainless steel manufactured by selective laser melting, Eng. Fract. Mech. 120 (2014) 15–25. doi:10.1016/j.engfracmech.2014.03.008.
[48] J.P. Strizak, H. Tian, P.K. Liaw, L.K. Mansur, Fatigue properties of type 316LN stainless steel in air and mercury, J. Nucl. Mater. 343 (2005) 134–144. doi:10.1016/j.jnucmat.2005.03.019.
[49] L. Ceschini, G. Minak, Fatigue behaviour of low temperature carburised AISI 316L austenitic stainless steel, Surf. Coatings Technol. 202 (2008) 1778–1784. doi:10.1016/j.surfcoat.2007.07.066.
[50] K. Tanaka, T. Mura, A theory of fatigue crack initiation at inclusions, Metall. Trans. A. 13A (1982) 117–123.
[51] M. Jaskari, J. Mäkikangas, A. Järvenpää, K. Mäntyjärvi, P. Karjalainen, Effect of high porosity on bending fatigue properties of 3D printed AISI 316L steel, Procedia Manuf. 36 (2019) 33–41. doi:10.1016/j.promfg.2019.08.006.
[52] D. Davidson, K. Chan, R. McClung, S. Hudak, Small fatigue cracks, in: Compr. Struct. Integr., Elsevier, 2003: pp. 129–164. doi:10.1016/B0-08-043749-4/04073-8.
[53] A.J. Wilkinson, S.G. Roberts, P.B. Hirsch, Modelling the threshold conditions for

propagation of stage I fatigue cracks, Acta Mater. 46 (1998) 379–390. doi:10.1016/S1359-6454(97)00290-5.
[54] A.J. Wilkinson, S.G. Roberts, A dislocation model for the two critical stress intensities required for threshold fatigue crack propagation, Scr. Mater. 35 (1996) 1365–1371. doi:10.1016/1359-6462(96)00301-6.
[55] M.H. El Haddad, T.H. Topper, K.N. Smith, Prediction of non propagating cracks, Eng. Fract. Mech. 11 (1979) 573–584. doi:10.1016/0013-7944(79)90081-X.
[56] P. Kumar, U. Ramamurty, High cycle fatigue in selective laser melted Ti-6Al-4V, Acta Mater. (2020). doi:10.1016/j.actamat.2020.05.041.
[57] T. Zhai, A.J. Wilkinson, J.W. Martin, A crystallographic mechanism for fatigue crack propagation through grain boundaries, Acta Mater. 48 (2000) 4917–4927. doi:10.1016/S1359-6454(00)00214-7.
[58] W. Schäf, M. Marx, A.F. Knorr, Influence of microstructural barriers on small fatigue crack growth in mild steel, Int. J. Fatigue. 57 (2013) 86–92. doi:10.1016/j.ijfatigue.2012.11.006.
[59] S. Suresh, R.O. Ritchie, Propagation of short fatigue cracks, Int. Met. Rev. 29 (1984) 445–475. doi:10.1179/imtr.1984.29.1.445.
[60] G.V. Prasad Reddy, C. Robertson, C. Déprés, M. Fivel, Effect of grain disorientation on early fatigue crack propagation in face-centred-cubic polycrystals: A three-dimensional dislocation dynamics investigation, Acta Mater. 61 (2013) 5300–5310. doi:10.1016/j.actamat.2013.05.021.
[61] S. Taira, K. Tanaka, Y. Nakai, A model of crack-tip slip band blocked by grain boundary, Mech. Res. Comm. 5 (1978) 375–381.
[62] D.A. Koss, K.S. Chan, On crack propagation along crystallographic slip bands, in: Dislocation Model. Phys. Syst., Elsevier, 1981: pp. 18–22. doi:10.1016/B978-0-08-026724-1.50006-6.
[63] K. Tanaka, Y. Nakai, M. Yamashits, Fatigue growth threshold of small cracks, Int. J. Fract. 17 (1981). doi:https://doi.org/10.1007/BF00033345.
[64] G. Hua, M.W. Brown, K.J. Miller, Mixed-mode fatigue thresholds, Fatigue Fract. Eng. Mater. Struct. 5 (1982) 1–17. doi:10.1111/j.1460-2695.1982.tb01220.x.
[65] K.G. Samuel, G. Sasikala, S.K. Ray, On R ratio dependence of threshold stress intensity factor range for fatigue crack growth in type 316(N) stainless steel weld, Mater. Sci. Technol. 27 (2011) 371–376. doi:10.1179/026708310X12699498463048.
[66] A. Ritchie, Threshold for fatigue crack propagation: questions and anomalies, in: Sixth Int. Conf. Fract., 1984. doi:https://escholarship.org/uc/item/9zz69426.
[67] T. Ishimoto, S. Wu, Y. Ito, S.-H. Sun, H. Amano, T. Nakano, Crystallographic orientation control of 316L austenitic stainless steel via selective laser melting, ISIJ Int. (2020) 1–7. doi:10.2355/isijinternational.ISIJINT-2019-744.
[68] O. Andreau, I. Koutiri, P. Peyre, J.D. Penot, N. Saintier, E. Pessard, T. De Terris, C. Dupuy, T. Baudin, Texture control of 316L parts by modulation of the melt pool morphology in selective laser melting, J. Mater. Process. Technol. 264 (2019) 21–31. doi:10.1016/j.jmatprotec.2018.08.049.

Table 1. Composition (in wt.%) of BJP and SLM specimens measured by wavelength dispersive spectroscopy (WDS). The data is average of point analysis performed on at least 7 different locations.

Specimen		Fe (wt.%)	Ni (wt.%)	Mo (wt.%)	Cr (wt.%)	Mn (wt.%)	Si (wt.%)
BJP	Matrix	69.8 ± 0.1	10.8 ± 0.1	1.9 ± 0.1	15.7 ± 0.1	1.16 ± 0.01	0.60± 0.01
	δ - Ferrite	66.9± 0.2	4.5 ± 0.1	4.3 ± 0.1	22.8 ± 0.2	0.93 ± 0.03	0.69 ± 0.01
SLM		65.7 ± 0.1	12.4 ± 0.2	2.28 ± 0.03	17.5 ± 0.1	1.32 ± 0.06	0.70 ± 0.01

Table 2. Tensile and fatigue properties of the BJP, SLM and CM specimens.

Material	Relative porosity (%)	Yield strength, σ_y (MPa)	UTS, σ_u (MPa)	Elongation to fracture, e_f (%)	Fatigue strength, σ_f (MPa)
BJP (P-series)	3.86	198 ± 4.8	556 ± 5.4	66 ± 6.2	250
	4.25	197 ± 3.5	555 ± 4.3	70 ± 2.6	
	4.87	189 ± 1	547 ± 0.5	70.5 ± 0.5	
	5.64	189 ± 1.7	534 ± 5	64 ± 2	
BJP (S-series)	3.7	196 ± 4	548 ± 6.5	80 ± 1	250
	4.2	196 ± 4.1	555 ± 8.2	75 ± 2	
	4.48	198 ± 1.6	558 ± 3.8	74 ± 3.6	
	4.69	196 ± 2.9	551 ± 4.3	75 ± 4.6	
SLM (P-orientation)	2.3	511 ± 14	621 ± 11	20 ± 2	101
SLM (S-orientation)	2.3	430 ± 11	510 ± 20	12 ± 1	-
CM	0	273 ± 37	622 ± 6	65 ± 10	-

Table 3. Material parameters obtained by fitting the Ludwigson constitutive models for the work hardening in BJP and CM specimens. For the purpose of comparison, the parameters obtained from literature for CM 316L with similar grains size, *d*, is also listed.

Ludwigson constants (Eq. 1) ⟶ / **Material** ↓		**K_1 (MPa)**	**n_1**	**K_2**	**n_2**
BJP	**P-series**	1296±55.18	0.536±0.012	4.966±0.087	-18.5±2
	S-series	1317±31.02	0.531±0.004	4.9575±0.064	-19.5±1.9
CM (this study)		1372±17	0.423±0.019	5.27±0.12	-29±2
CM (literature) [42]		1291.7	0.37	5.2	-54

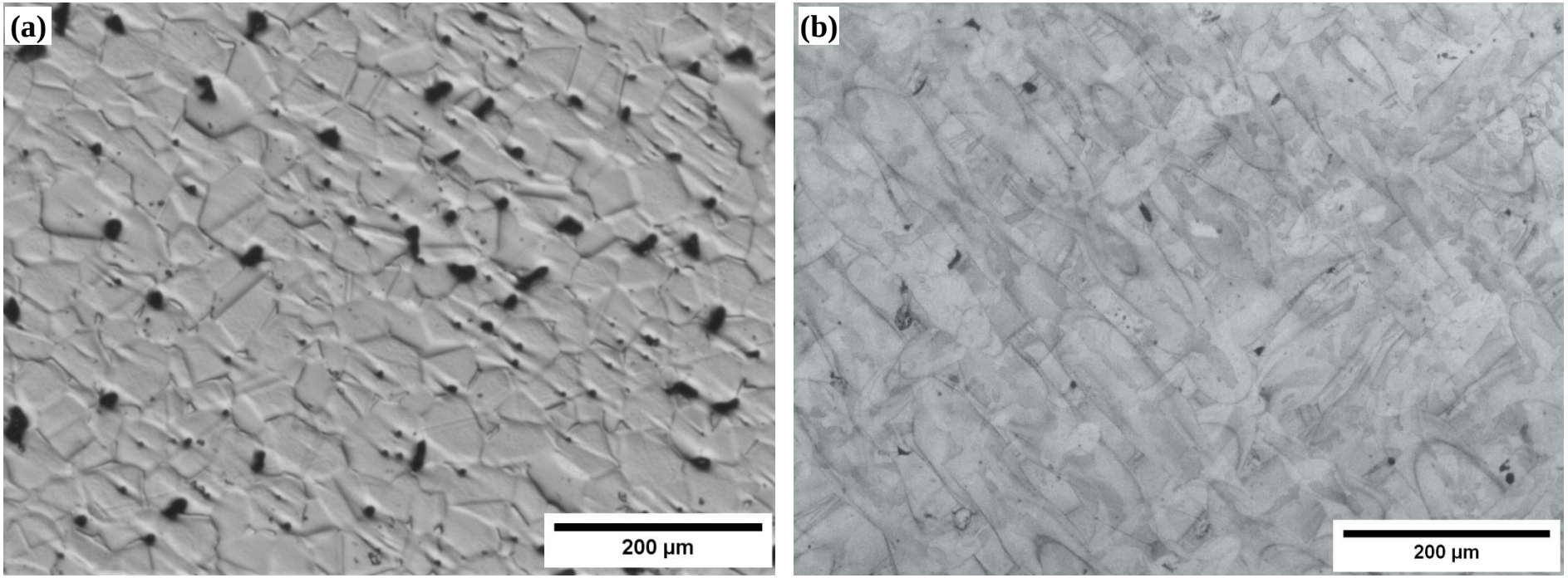

Figure 1. Optical micrographs showing the representative microstructures of 316L austenitic stainless steel alloy manufactured using (a) binder jet printing, and (b) selective laser melting. Fig. (b) shows the top view (of the plane perpendicular to the build direction of the SLM alloy).

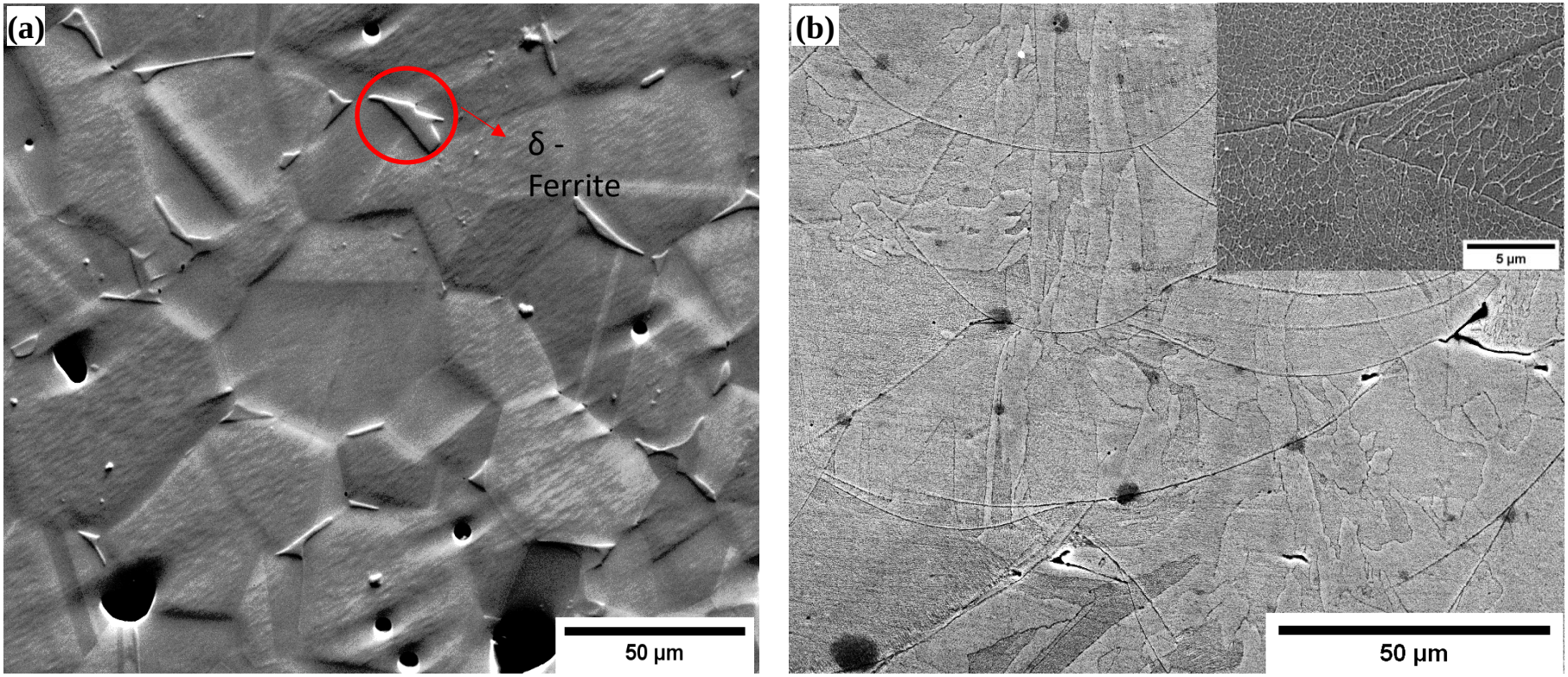

Figure 2. Scanning electron micrographs showing representative microstructures of 316L austenitic stainless steel alloy manufactured using (a) binder jet printing, and (b) selective laser melting. Fig. (b) shows the side view (of the plane parallel to the build direction of the SLM alloy). The red circle in (a) highlights a δ-ferrite precipitate. Inset in (b) shows the fine solidification cell structure present in the SLM specimens.

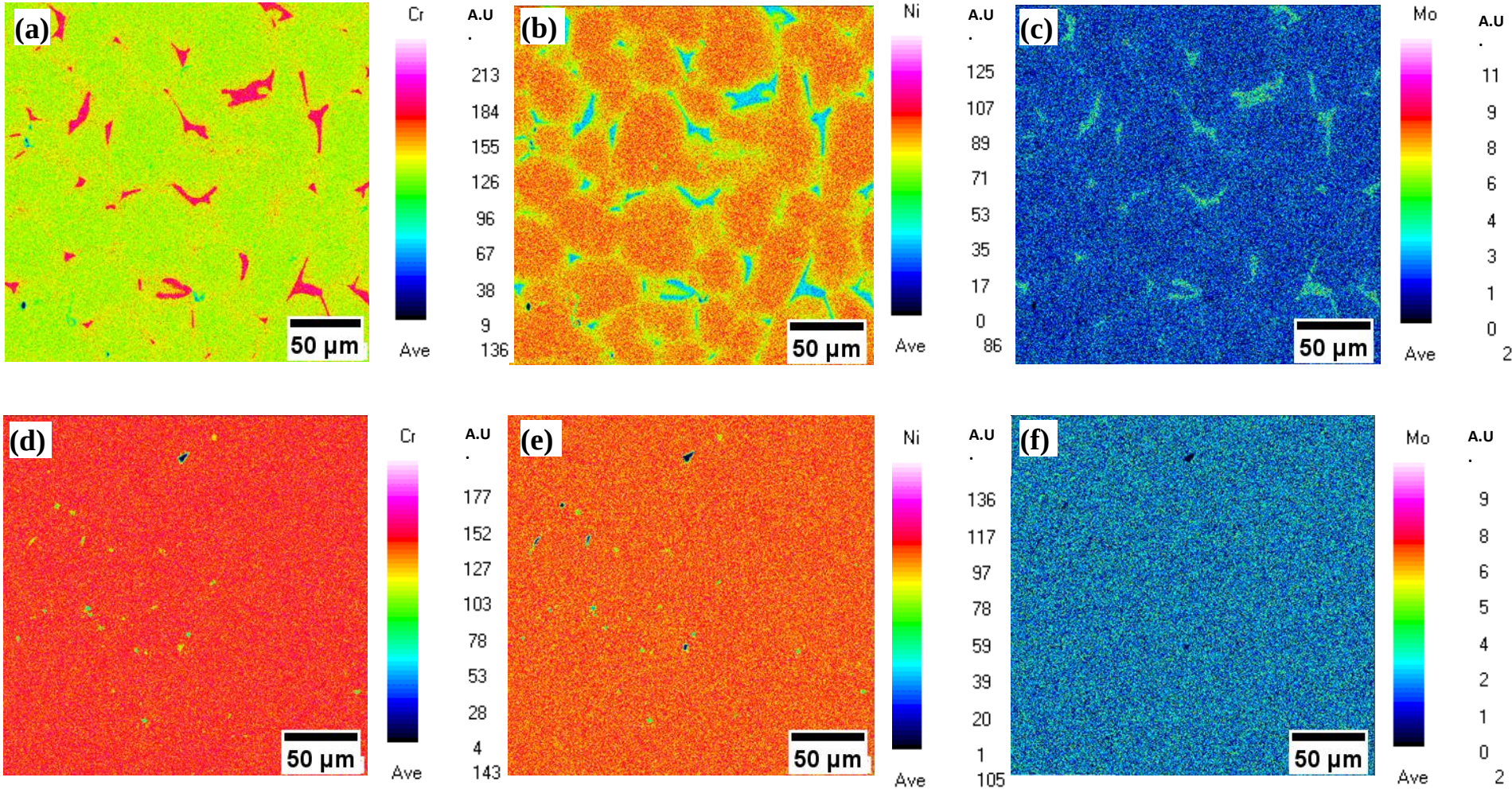

Figure 3. Wavelength dispersive spectroscopic (WDS) analyses of BJP (top row) and SLM (bottom row) specimens showing distributions of (a, d) Cr (b, e) Ni and (c, f) Mo in the Fe matrix. Note the segregation of Cr an Mo and depletion of Ni at the grain boundaries in the BJP specimens.

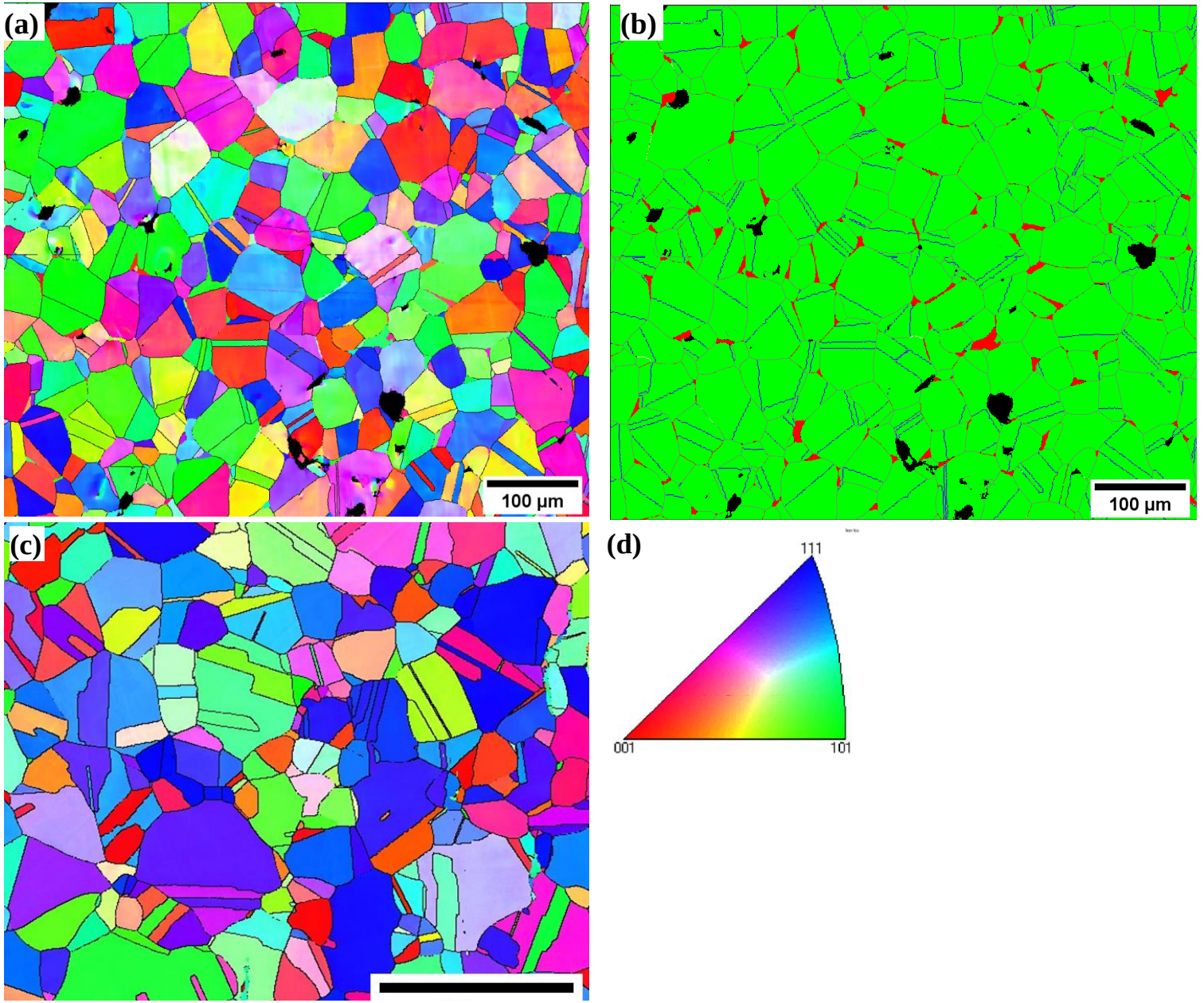

Figure 4. Representative images obtained using EBSD; (a) IPF map obtained from a BJP specimen, which illustrates the orientation distribution of the grains, and (b) a phase map, which shows a homogeneous distribution of the δ–ferrite (red) phase in the γ–austenite matrix (green). The blue lines in (b) indicate the presence of <111> 60° annealing twin boundaries. (c) An IPF map of CM specimen, (d) Legend for the IPF maps.

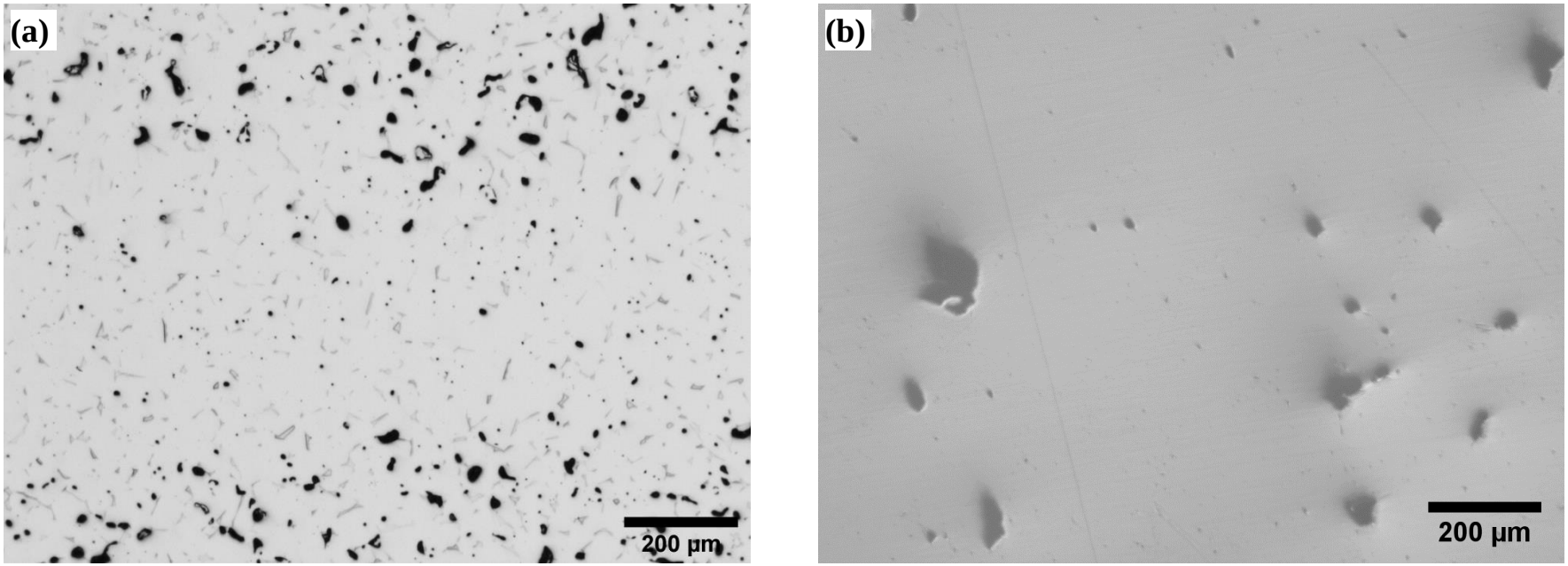

Figure 5. Representative optical micrographs showing porosity distribution in (a) BJP and (b) SLM specimens.

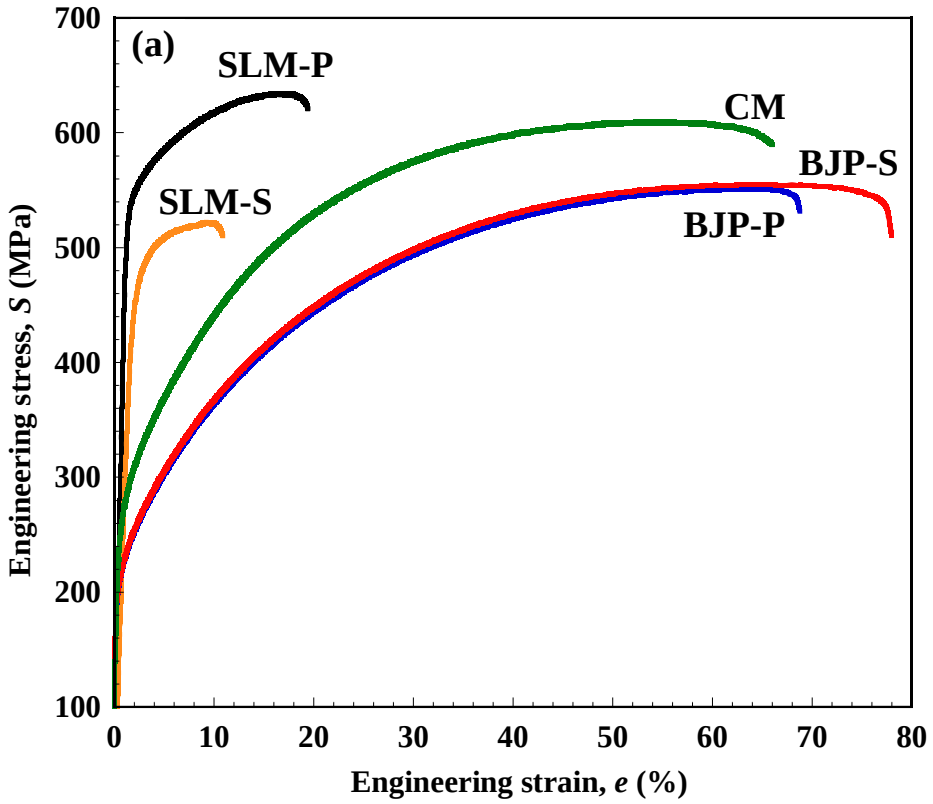

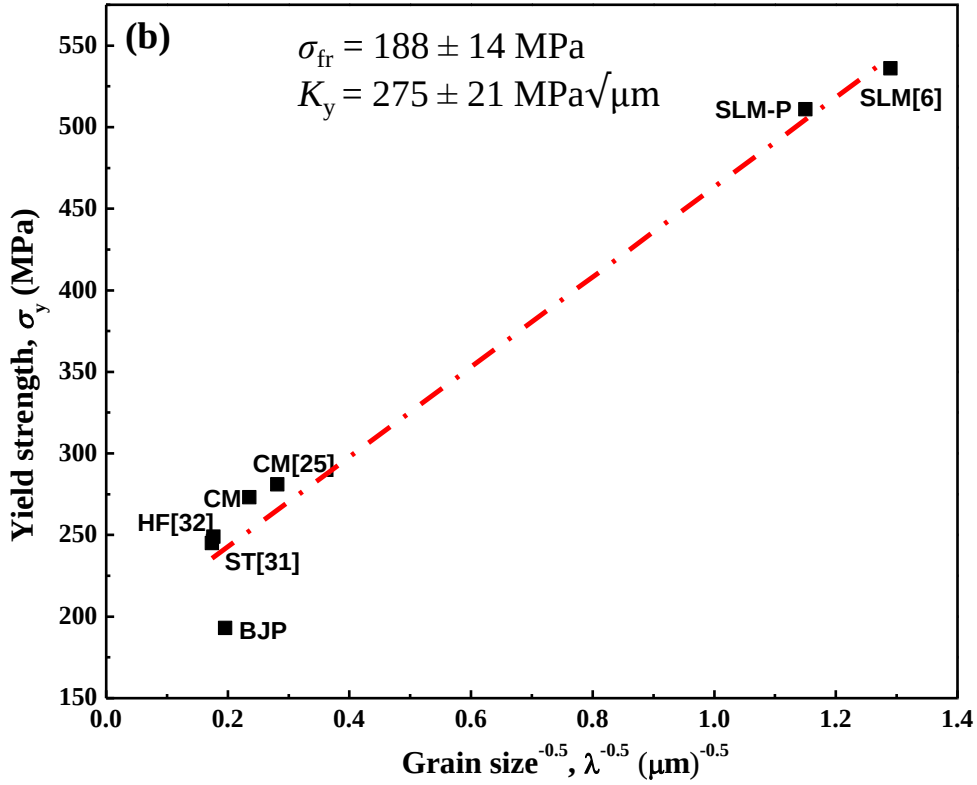

Figure 6. (a) Representative tensile stress-strain responses of SLM, BJP and CM specimens. (b) Yield strength versus grain size plot for data obtained on 316L SS manufactured by different processes, as per the Hall-Petch relation.

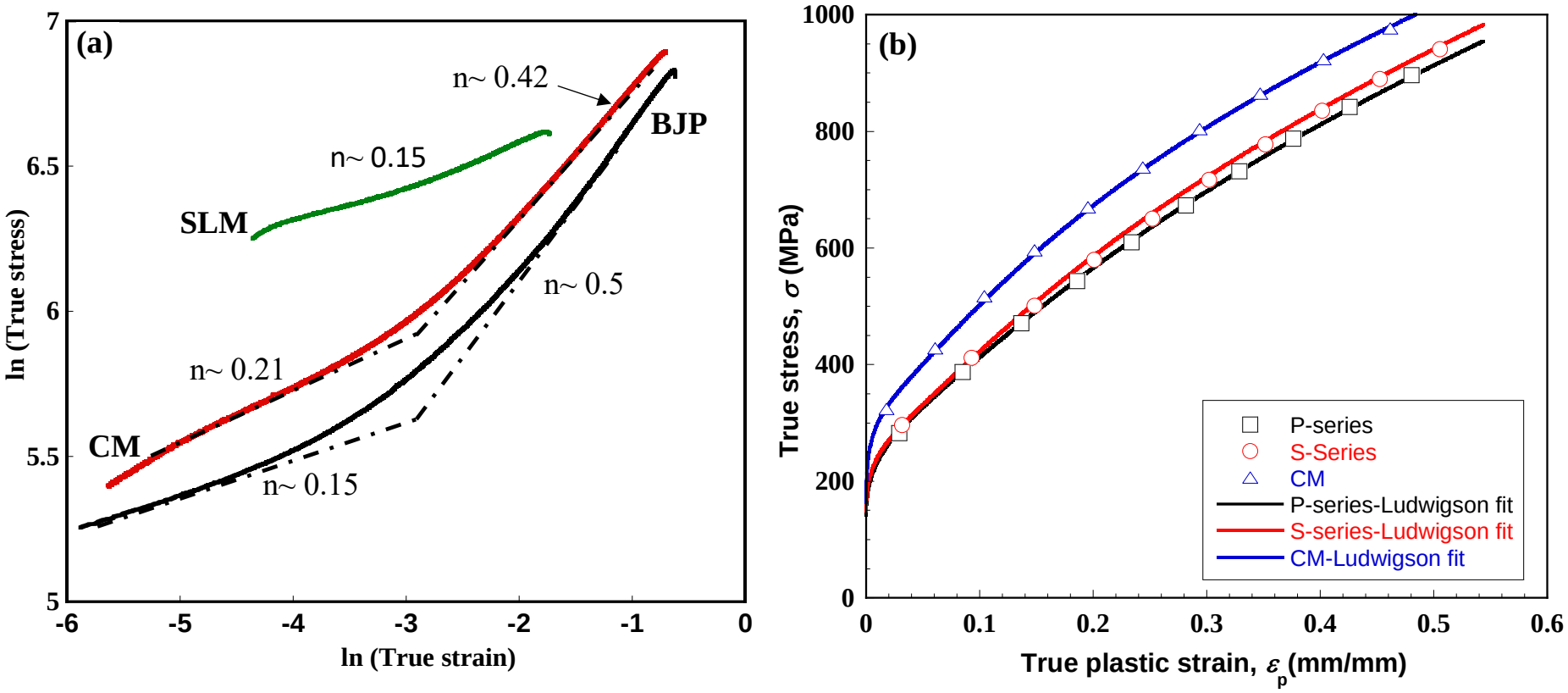

Figure 7. (a) Work hardening behavior of the BJP, SLM and CM specimens, showing the two stage hardening in BJP and CM specimens. (b) Experimental true stress vs. true plastic strain data fitted using the Ludwigson constitutive model.

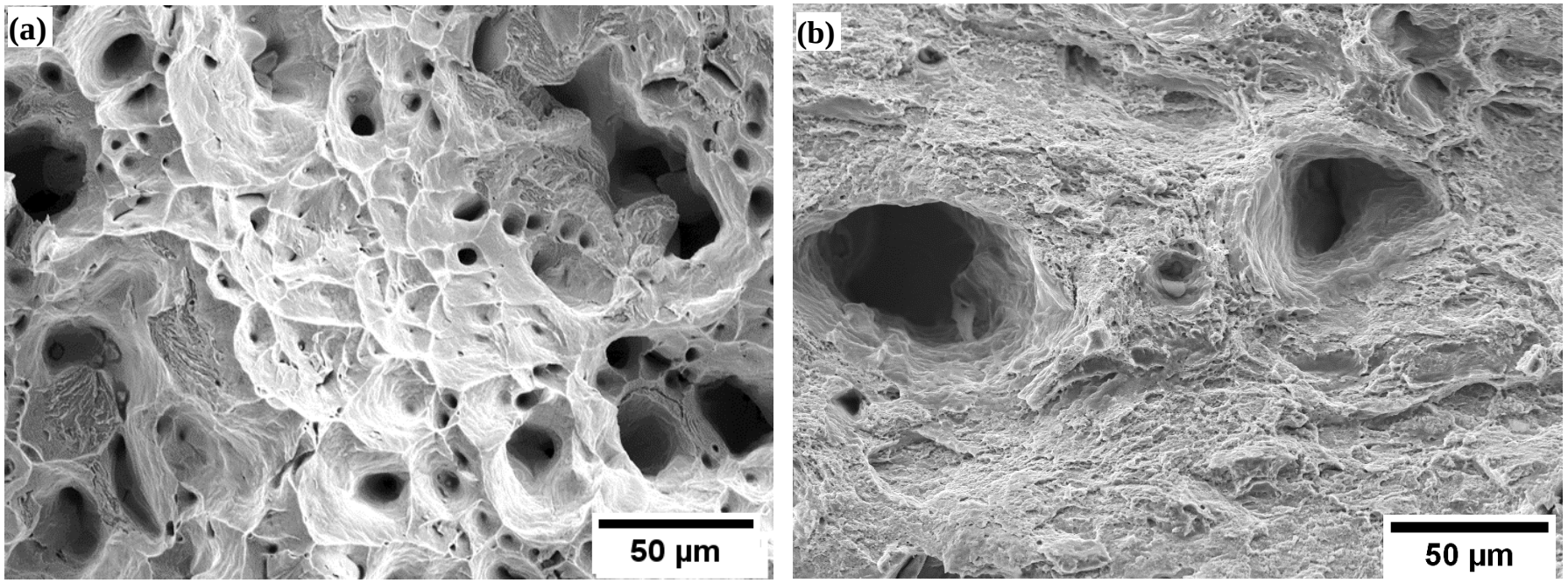

Figure 8. Fractographs obtained from the tensile tested samples showing (a) ductile fracture in a BJP sample showing large voids, and (b) fracture features in a SLM specimen.

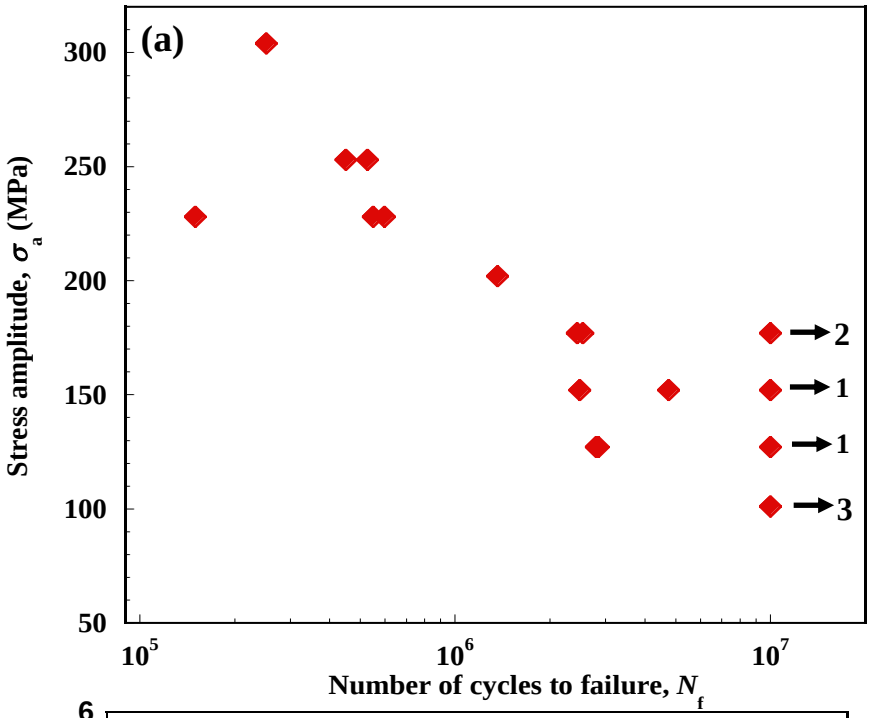

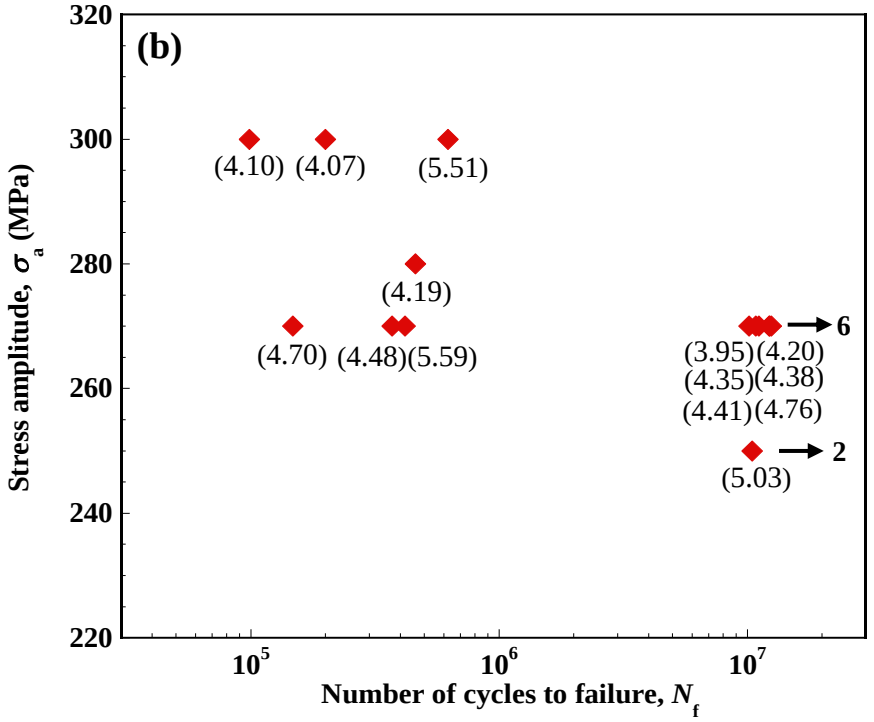

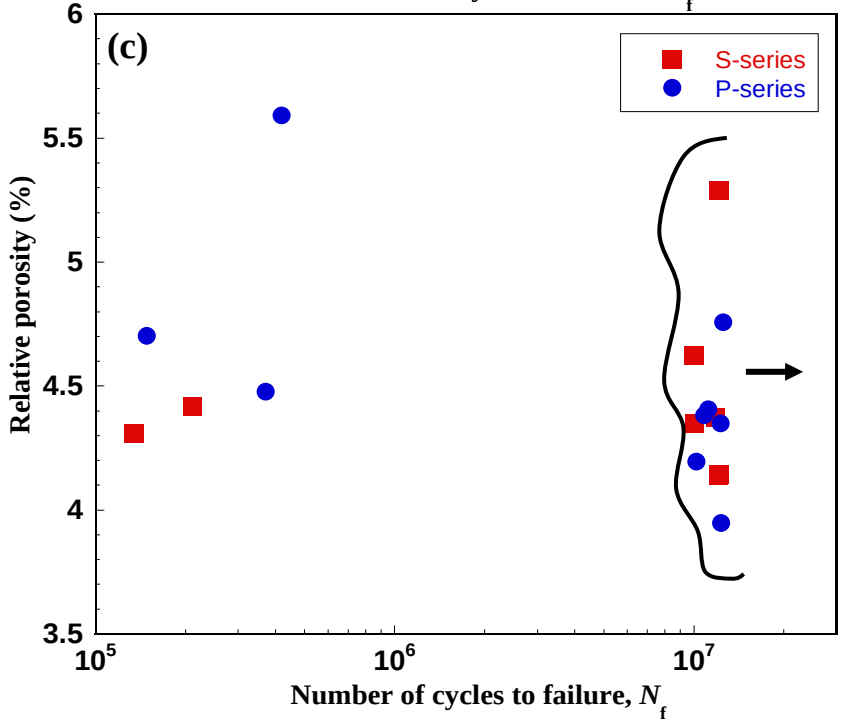

Figure 9. Stress amplitude (σ_a) versus number of cycles to failure (N_f) data obtained on (a) SLM and (b) BJP (P-series) specimens. (c) Results of the fatigue tests conducted at σ_a = 270 MPa on the specimens with different porosity levels. The data in the parentheses shown in (b) give the relative porosity (in %) of the sample. The arrows indicate run out specimens, i.e., those that did not fail even after 10^7 cycles, and the numbers next to the arrows indicate the number of specimens that survived at that stress amplitude.

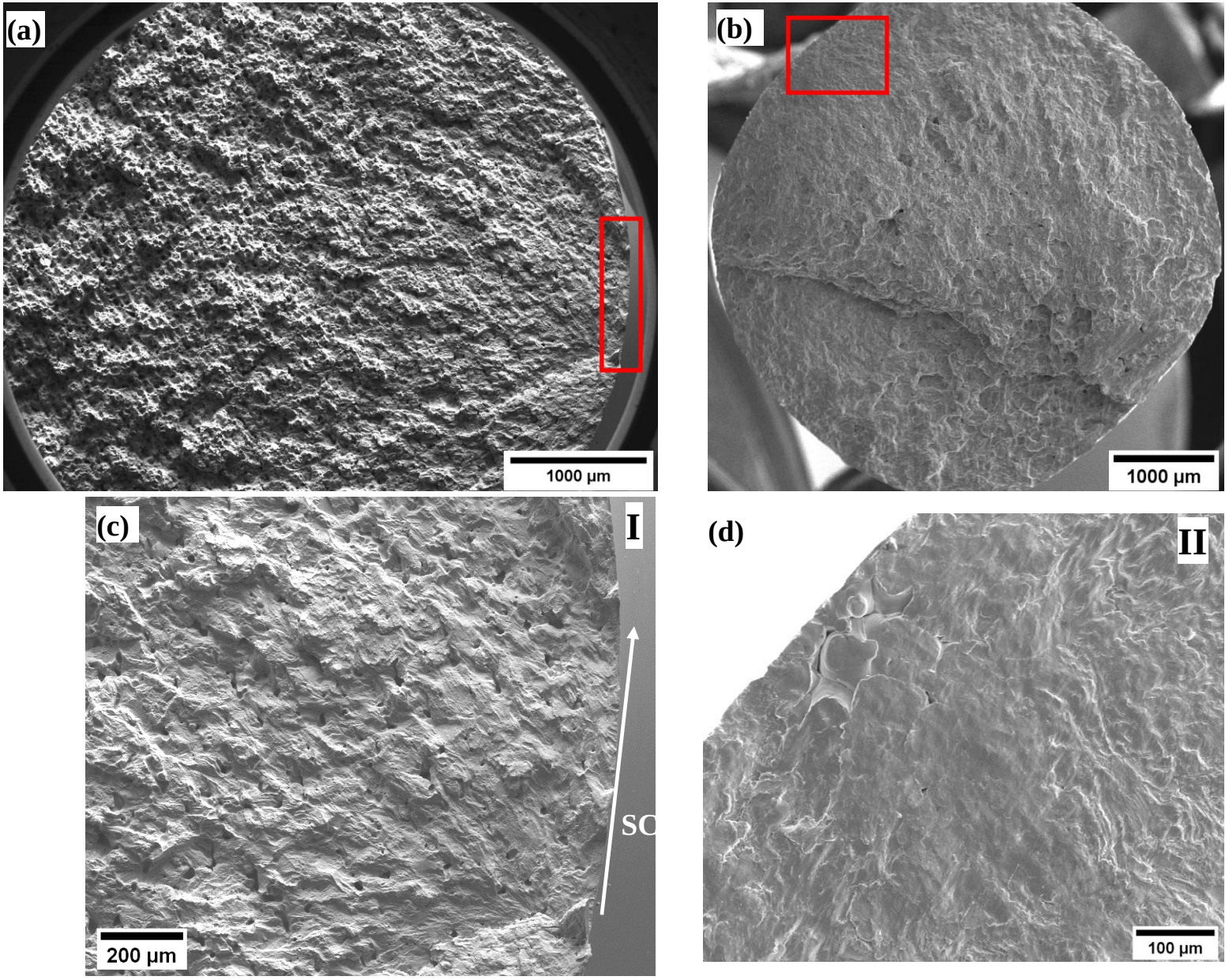

Figure 10. The fracture surfaces of (a) BJP Specimen fatigued at stress amplitude, σ_a, 300 MPa, number of cycles to failure, N_f, 98368 (b) SLM specimen fatigued at σ_a, 152 MPa, N_f, 2.5×10^5. High magnification image showing crack initiating from the (c) surface of BJP specimen, and (d) from the pores near the surface in the SLM specimen. The arrow in (c) shows the direction of growth of the small fatigue crack along the surface.

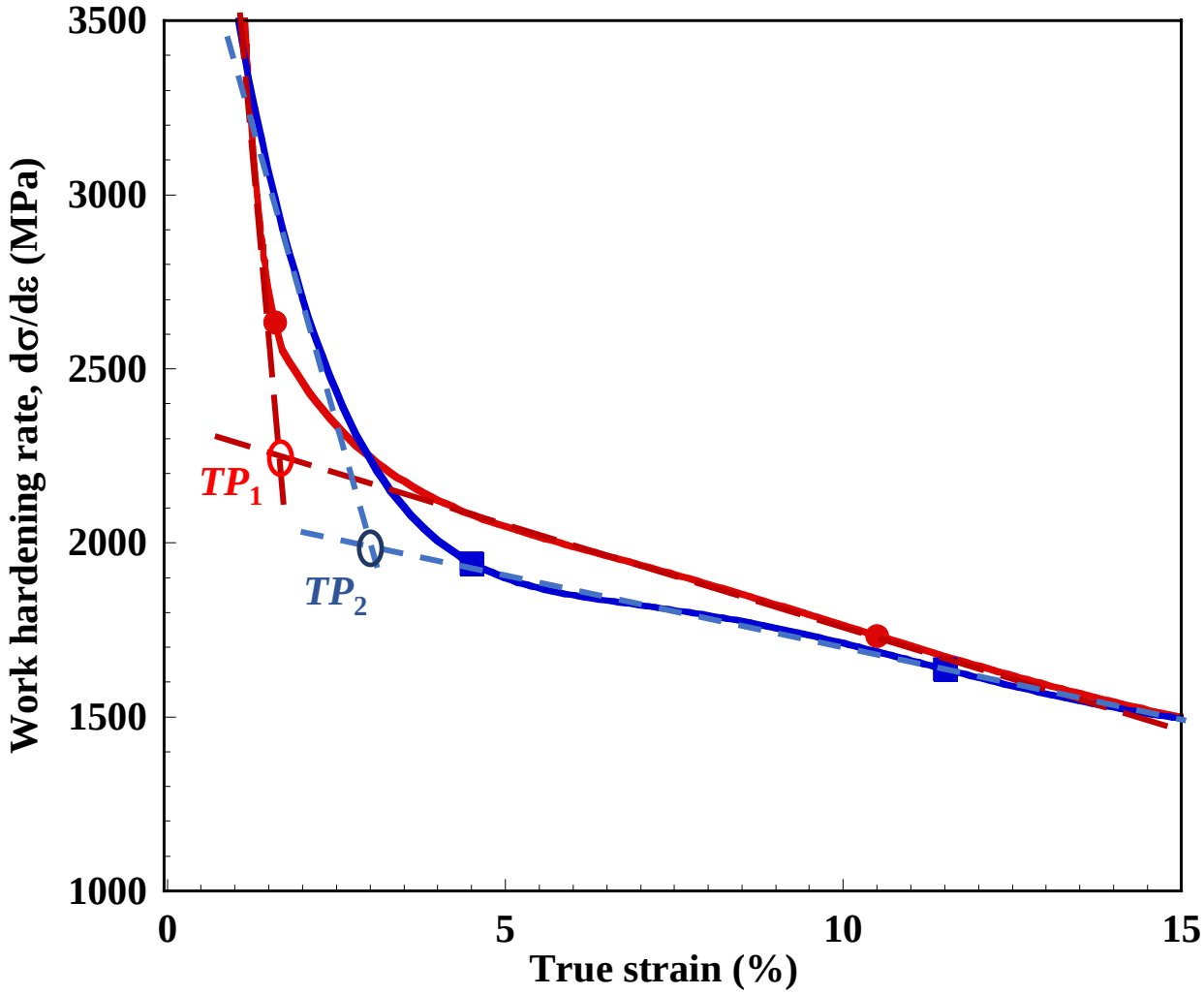

Figure 11. Work hardening rate, dσ/dε, plotted as a function of the true strain for the BJP and CM specimens, showing the transition from planer glide to cross-slip. Points TP_1 and TP_2 corresponds to true strain, ε_T, where transition from planer glide to duplex slip starts in the CM and BJP specimens respectively.

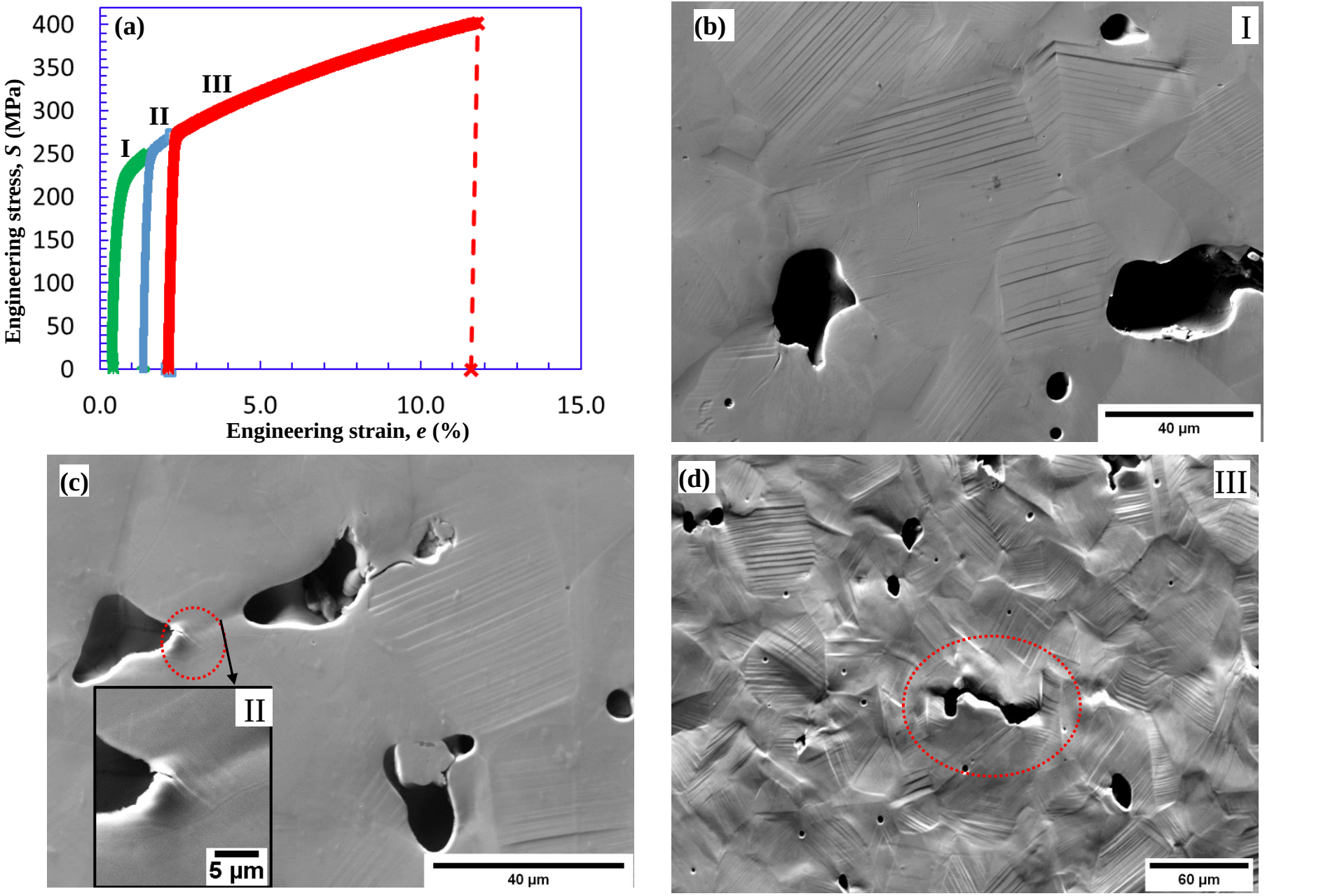

Figure 12. (a) Engineering stress, *S*, vs. strain, *e*, response recorded during the interrupted sub-sized tensile test of the BJP specimen. Microstructure of the specimen deformed to *e*, of (b) 1.36%, (c) 2.14%, and (d) 11.56%, which correspond to S, 250, 270 and 400 MPa, respectively. Red circles in (c) highlights the crack initiation from a pore along a slip trace, and in (d) crack blunting due to duplex slip in the grains near a pore.

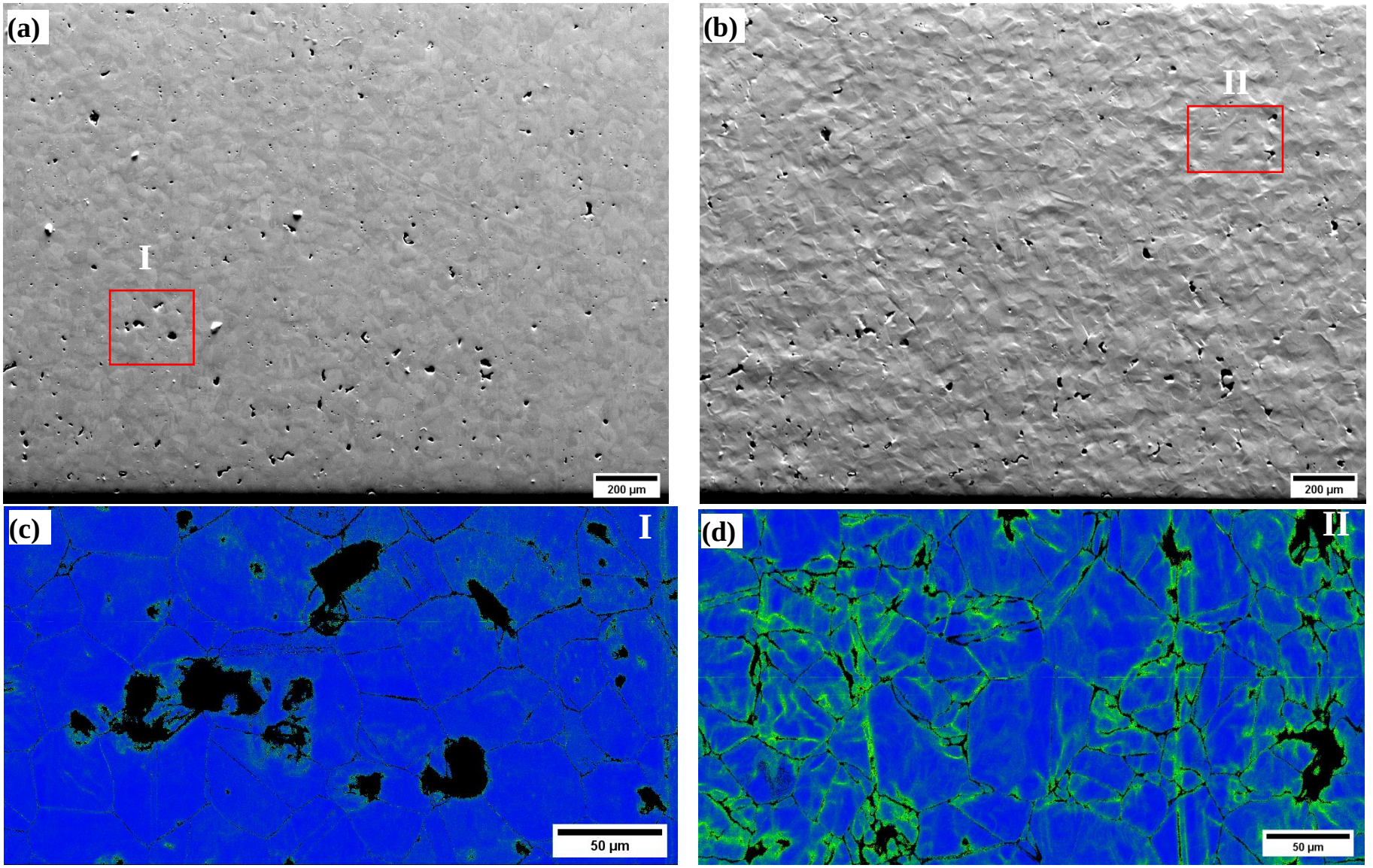

Figure 13. Microstructures of BJP specimen in (a) the undeformed state, and (b) after 4% engineering strain, *e*, which correspond to engineering stress, *S*, 300 MPa. EBSD Kernel average misorientation (KAM) map obtained from (c) region I of the undeformed specimen, and (d) region II of the deformed specimen.

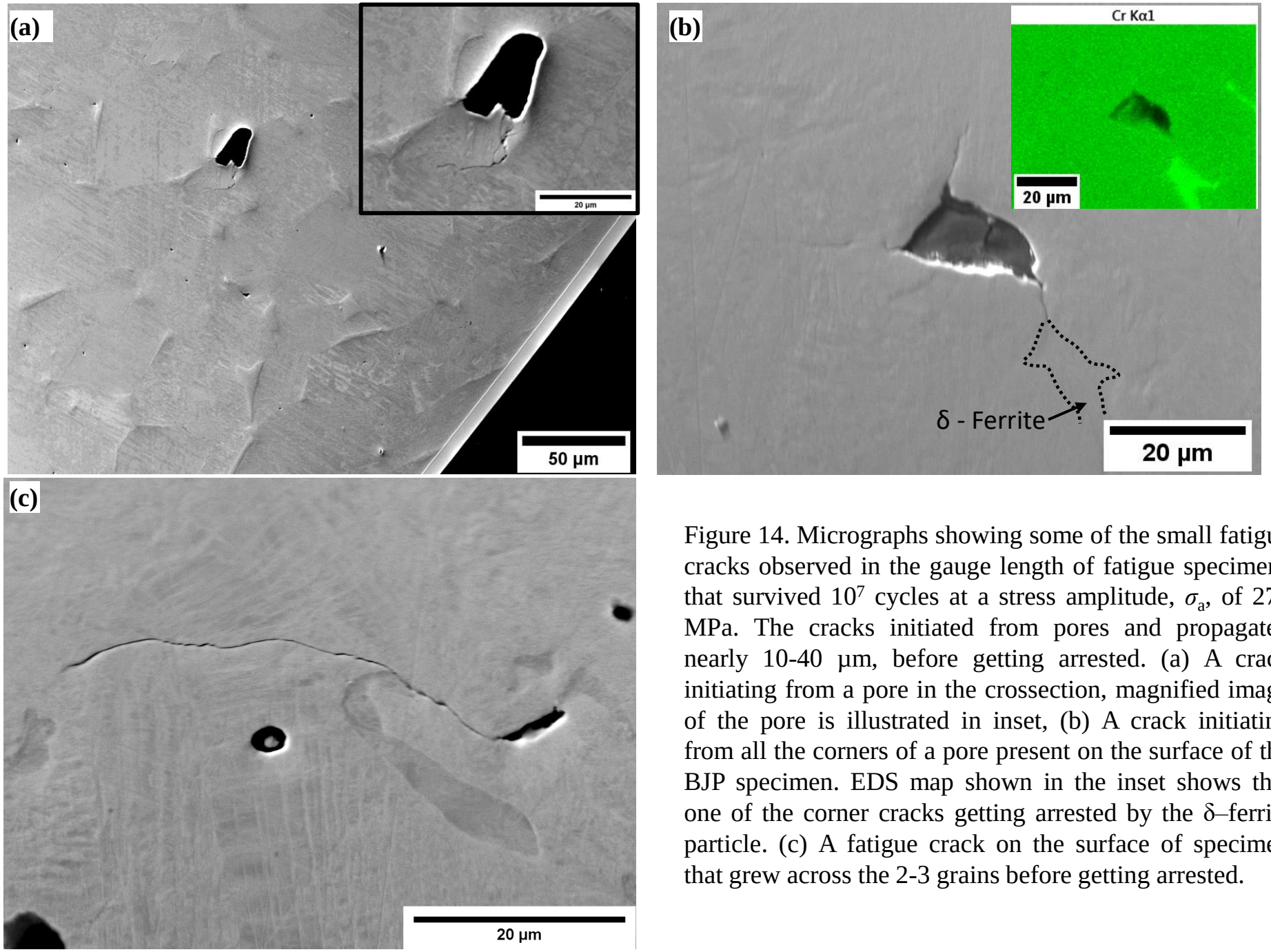

Figure 14. Micrographs showing some of the small fatigue cracks observed in the gauge length of fatigue specimens that survived 10^7 cycles at a stress amplitude, σ_a, of 270 MPa. The cracks initiated from pores and propagated nearly 10-40 µm, before getting arrested. (a) A crack initiating from a pore in the crossection, magnified image of the pore is illustrated in inset, (b) A crack initiating from all the corners of a pore present on the surface of the BJP specimen. EDS map shown in the inset shows that one of the corner cracks getting arrested by the δ–ferrite particle. (c) A fatigue crack on the surface of specimen that grew across the 2-3 grains before getting arrested.

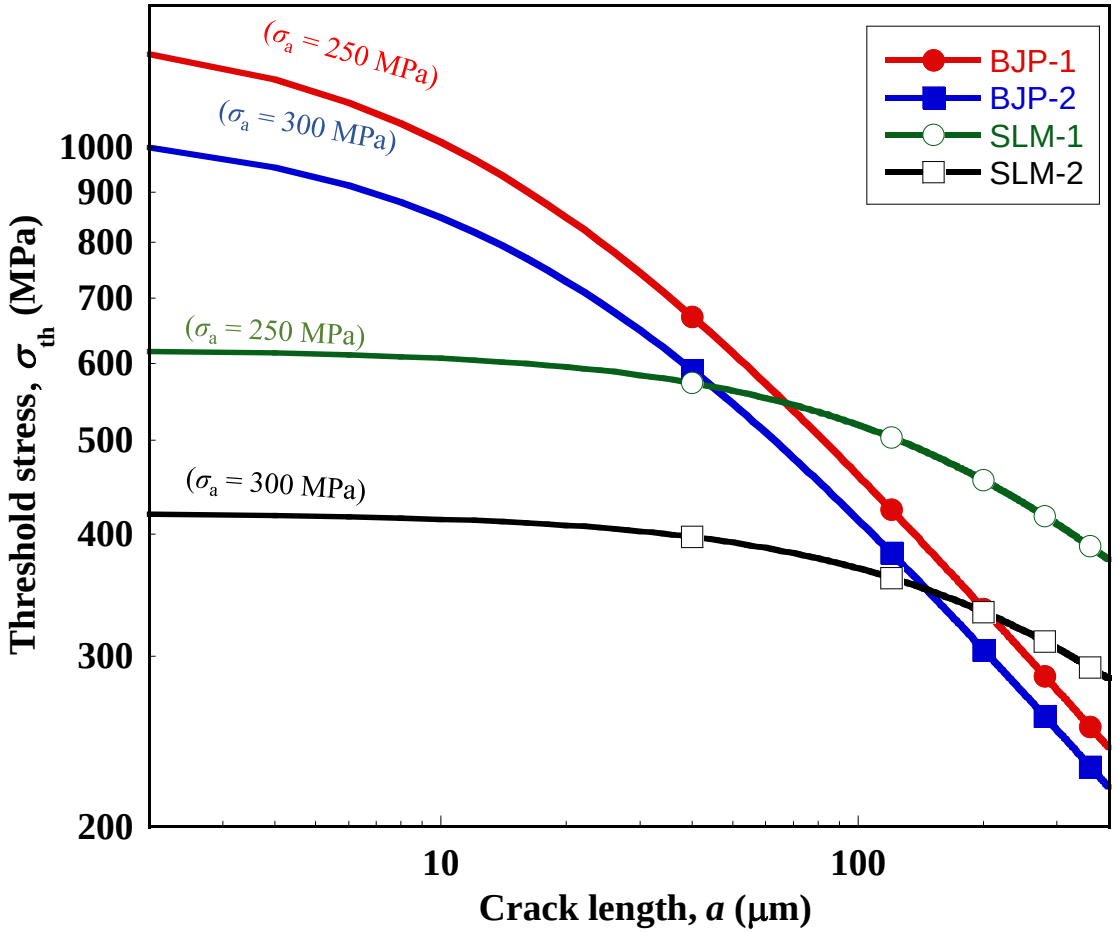

Figure 15. The variation in the threshold stress, σ_{th} for the propagation of a small fatigue cracks (SFC) across a grain boundary in BJP and SLM specimens fatigued at the stress amplitudes, σ_a, of 250 and 300 MPa. The σ_{th} was calculated using blocked slip band (BSB) theory.

Supplementary Information

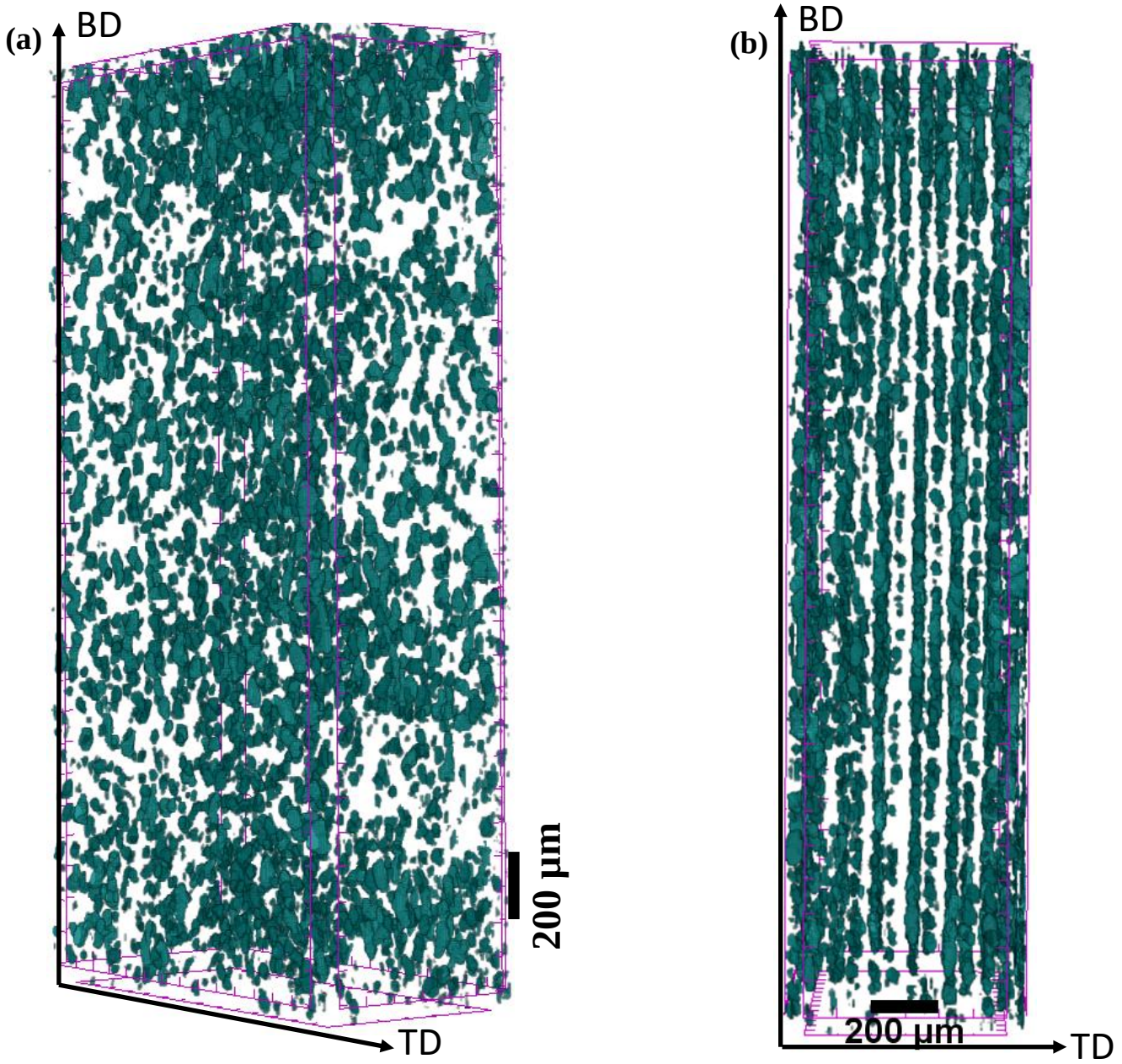

Figure S1. X-ray micro CT reconstruction showing (a) three dimensional porosity distribution, and (b) side view of the porosity distribution in BJP specimens. Distance between two adjacent markers in all the directions is 100 µm.

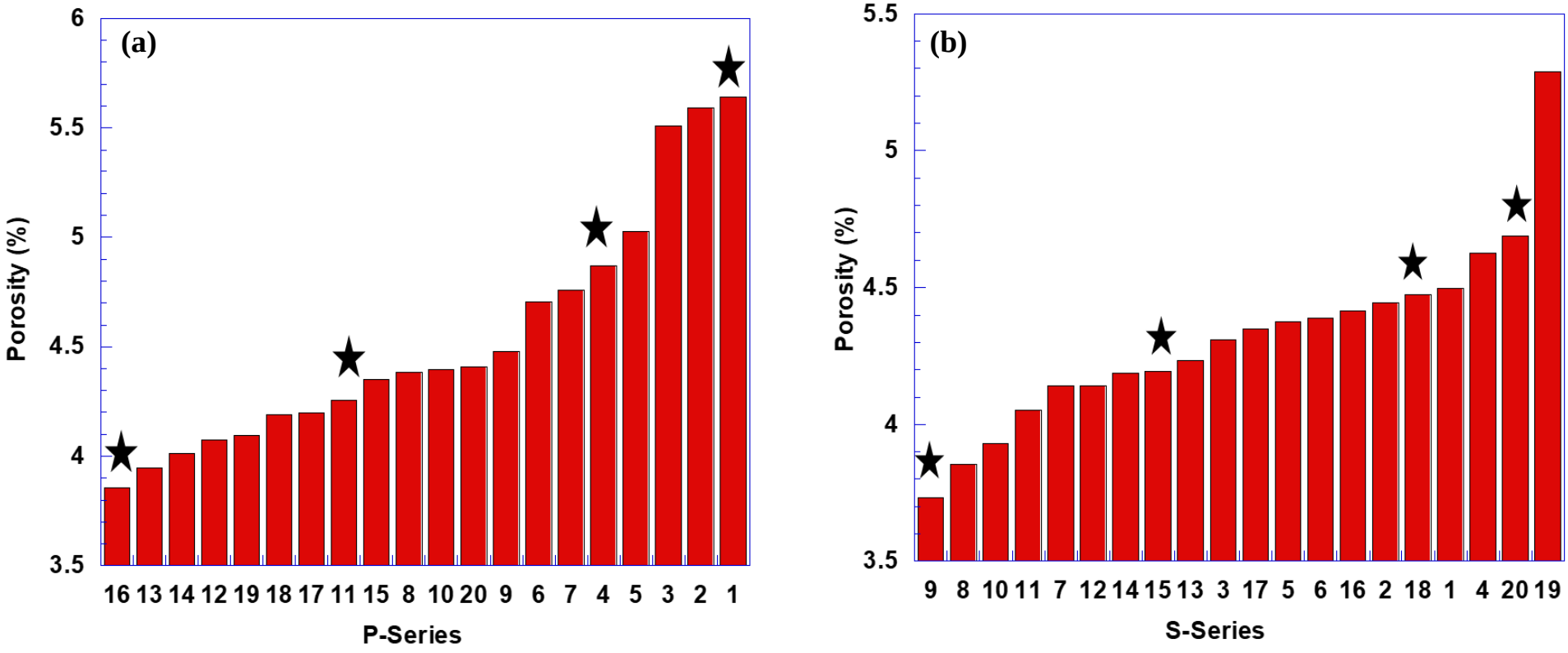

Figure S2. The bar chart showing the porosity distribution in (a) P-series, and (b) S-series of BJP specimens. The star mark above the bar indicates that these specimens were selected for tensile testing.

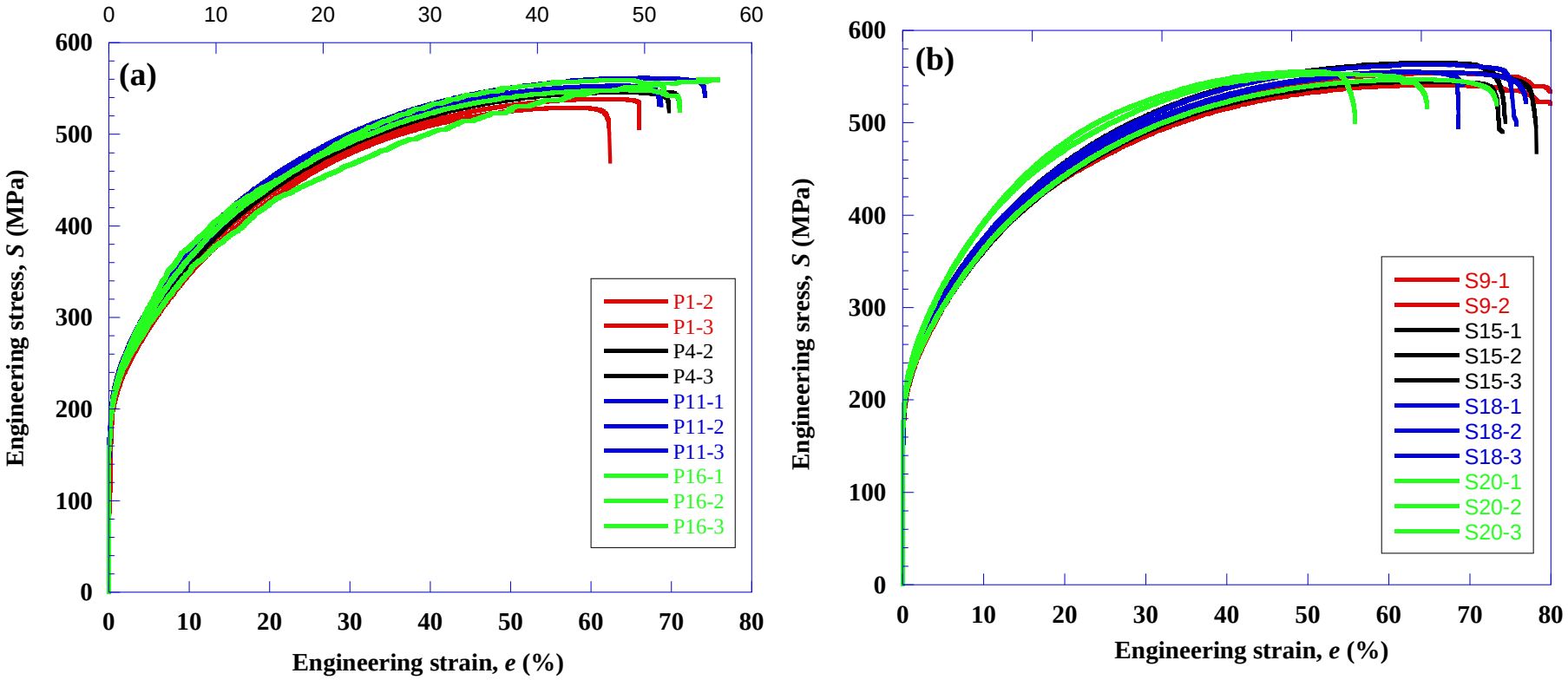

Figure S3. Representative tensile stress-strain responses of the various BJP 316L samples.

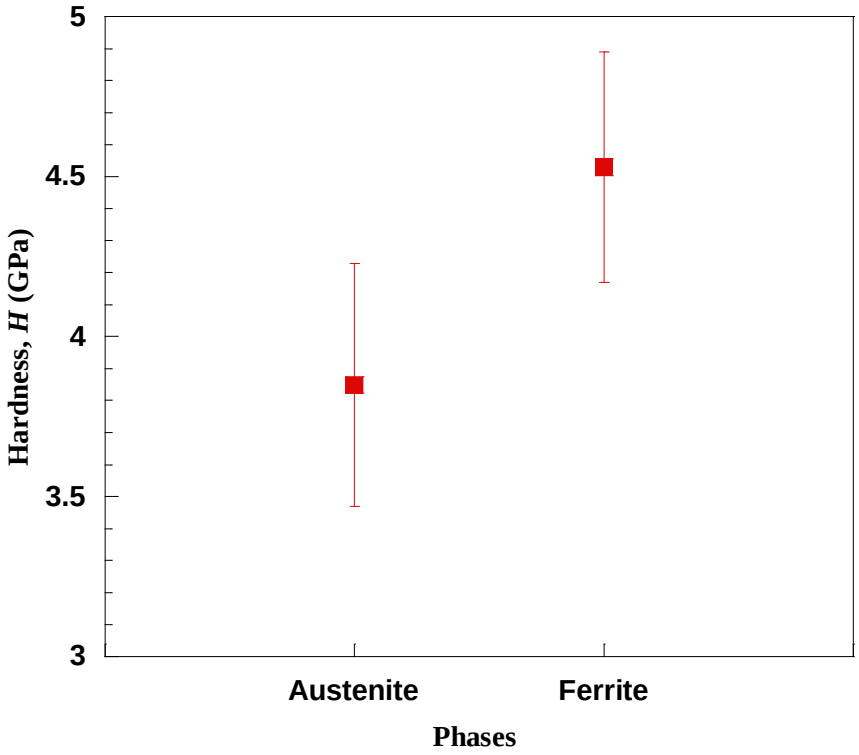

Figure S4. Hardness value obtained from the nano-indentation of phases in BJP specimens, γ – austenite and δ – Ferrite.

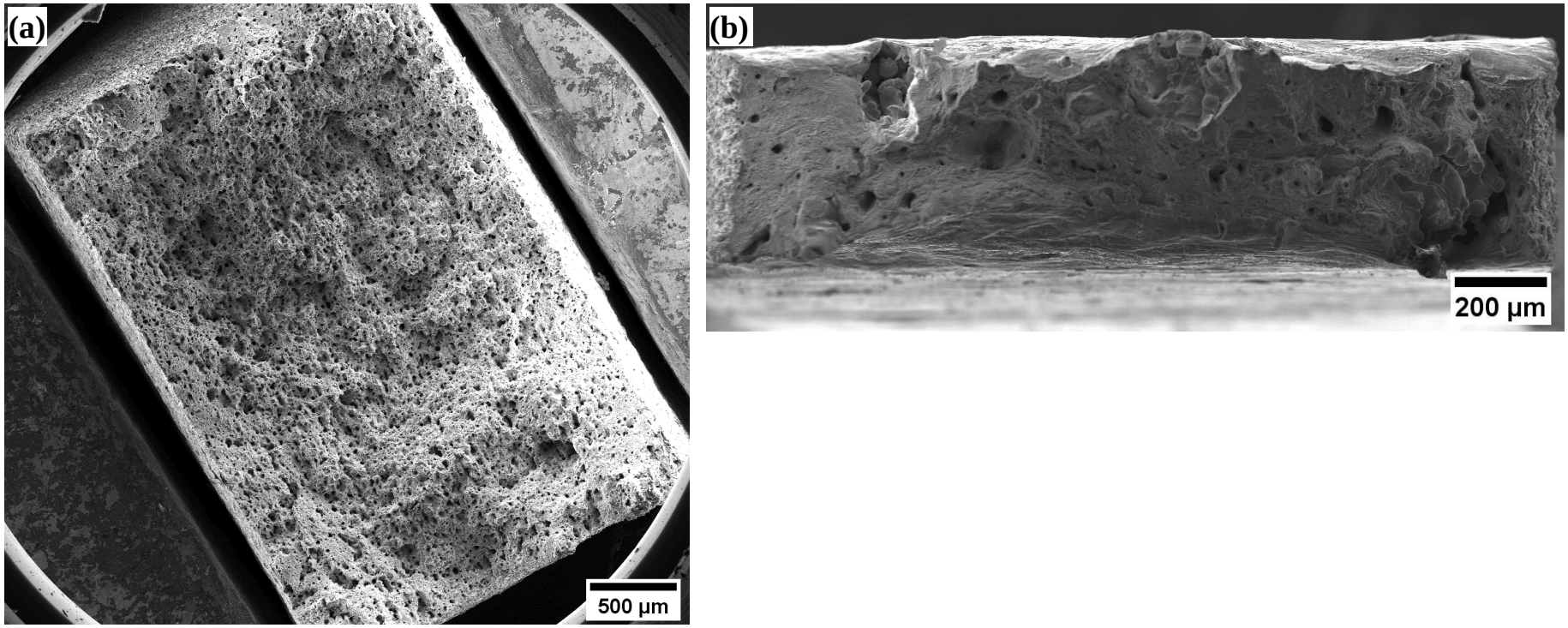

Figure S5. Fractographs obtained from the tensile tested samples of (a) BJP, and (b) SLM 316L

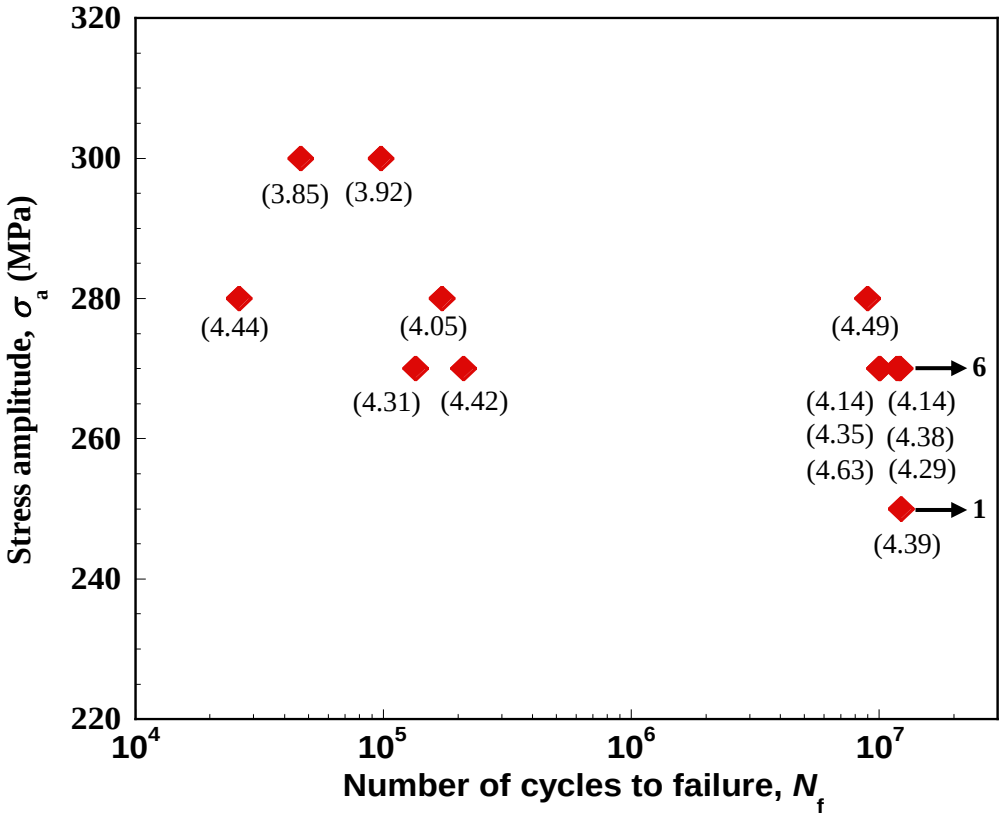

Figure S6. S-N curves of the specimen showing the fatigue strength, σ_f in BJP specimens (S-series).

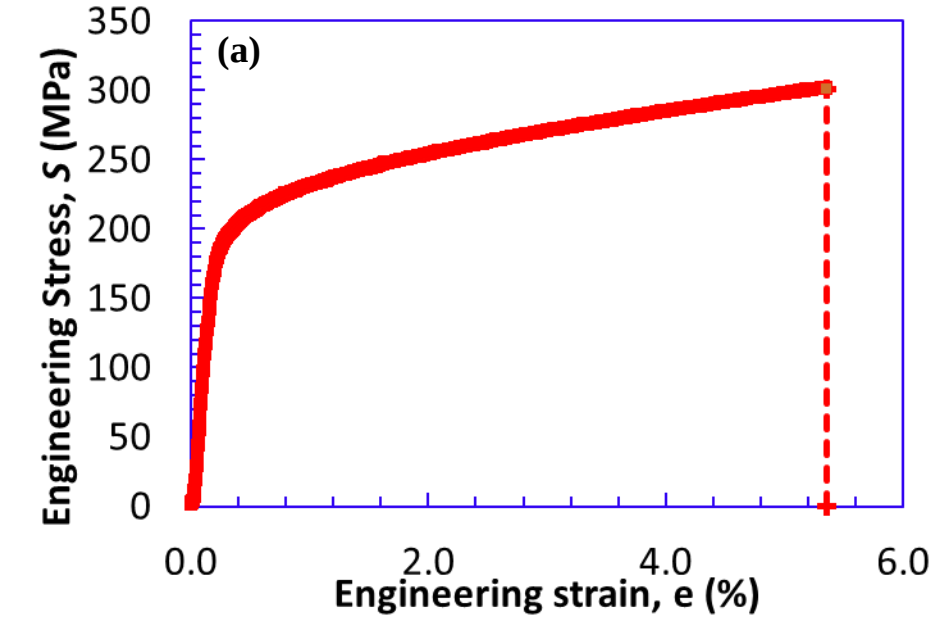

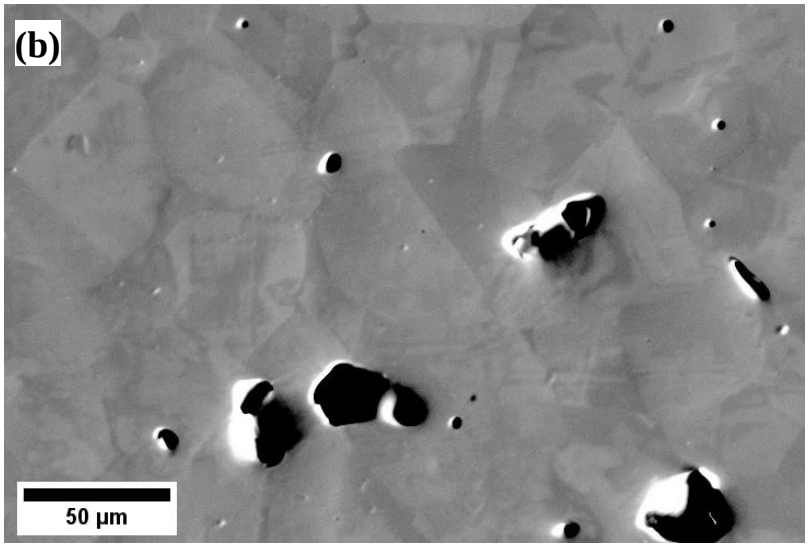

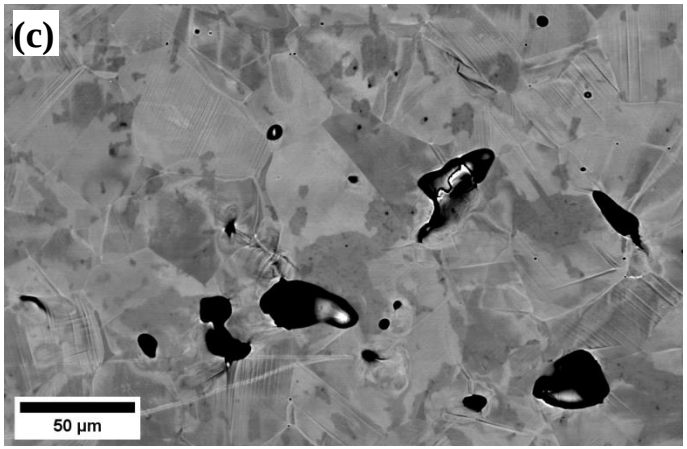

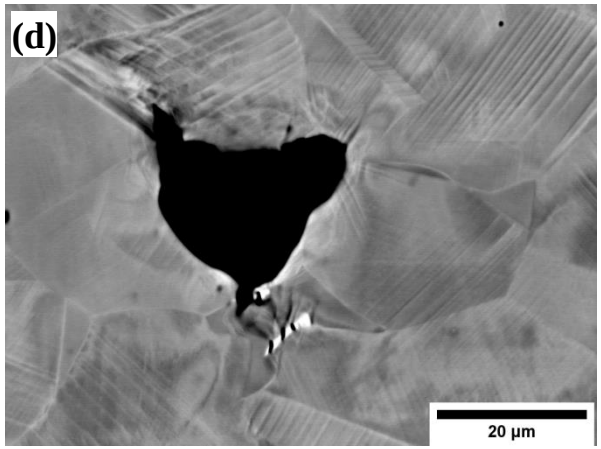

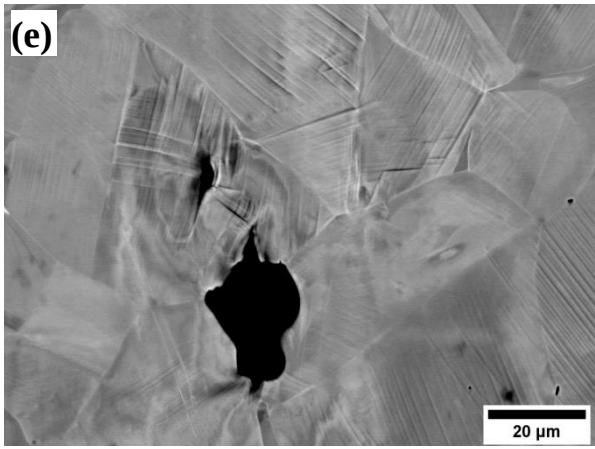

Figure S7. (a) Interrupted tensile stress-strain response of BJP specimens till engineering stress, *S*, 300 MPa corresponding to engineering strain, *e*, 4%, and microstructure in (b) un-deformed state (c) deformed up to *S*, 300 MPa, high magnification images showing duplex slip bands forming near the pores in (d) and (e), which is blunting the crack tips.